JEM Journal of Experimental Medicine

ARTICLE

Targeting MAPK phosphorylation of Connexin43 provides neuroprotection in stroke

Moises Freitas-Andrade[1], Nan Wang[2], John F. Bechberger[1], Marijke De Bock[2], Paul D. Lampe[3*], Luc Leybaert[2*], and Christian C. Naus[1*]

Connexin43 (Cx43) function is influenced by kinases that phosphorylate specific serine sites located near its C-terminus. Stroke is a powerful inducer of kinase activity, but its effect on Cx43 is unknown. We investigated the impact of wild-type (WT) and knock-in Cx43 with serine to alanine mutations at the protein kinase C (PKC) site $Cx43^{S368A}$, the casein kinase 1 (CK1) sites $Cx43^{S325A/328Y/330A}$, and the mitogen-activated protein kinase (MAPK) sites $Cx43^{S255/262/279/282A}$ (MK4) on a permanent middle cerebral artery occlusion (pMCAO) stroke model. We demonstrate that MK4 transgenic animals exhibit a significant decrease in infarct volume that was associated with improvement in behavioral performance. An increase in astrocyte reactivity with a concomitant decrease in microglial reactivity was observed in MK4 mice. In contrast to WT, MK4 astrocytes displayed reduced Cx43 hemichannel activity. Pharmacological blockade of Cx43 hemichannels with TAT-Gap19 also significantly decreased infarct volume in WT animals. This study provides novel molecular insights and charts new avenues for therapeutic intervention associated with Cx43 function.

Introduction

Ischemic stroke is a complex event characterized by cell death resulting from a transient or permanent arterial occlusion (Sacco et al., 2013). Astrocytic connexin43 (Cx43) gap junction (GJ) channels have been reported to impact neuronal survival in ischemic conditions (Siushansian et al., 2001; Nakase et al., 2004; Kozoriz et al., 2010), but Cx43 knockout versus pharmacological inhibition of Cx43 has often produced divergent outcomes (reviewed in Schulz et al., 2015). Astrocyte GJs are composed primarily of the channel protein Cx43 and, to a lesser extent, Cx30 and Cx26 (Naus et al., 1991; Giaume, 1996). Cx43 protein hexamers form transmembrane channels, termed connexons, which then couple with apposing connexons on neighboring cells and coalesce into dense GJ plaques. Astrocytic cell networks coupled by Cx43 GJs allow for the intercellular exchange of metabolites and second messengers (Goodenough and Paul, 2009). However, Cx43 channels also form hemichannels that connect the cell cytoplasm to the extracellular milieu (Orellana et al., 2009; Giaume et al., 2013). Hemichannels are mostly active under pathological conditions and facilitate the entry of Na^+ and Ca^{2+} into the cell and the escape of K^+, ATP, and other molecules, potentially contributing to autocrine/paracrine signaling but also leading to the loss of essential metabolites (Chever et al., 2014; D'hondt et al., 2014; Schulz et al., 2015).

The C-terminus (CT) of Cx43 plays a key role in channel function, harboring putative phosphorylation sites specific to different kinases that directly regulate Cx43 activity (Solan and Lampe, 2009; Chen et al., 2013; Pogoda et al., 2016). Interestingly, mice expressing a truncated mutant form of Cx43 lacking the CT (Cx43ΔCT; truncation at amino acid 258), exhibited increased stroke damage and inflammation (Kozoriz et al., 2010). The deletion was shown to have a dominant negative effect in ischemic damage in mice expressing both WT and Cx43ΔCT alleles (Kozoriz et al., 2010), underscoring the critical role Cx43 CT plays in stroke.

Ischemia activates cellular kinases, several of which have been linked with Cx43. We tested whether Cx43 phosphorylation–null mutants show significant differences to permanent middle cerebral artery occlusion (pMCAO). WT and knock-in mice containing null phosphorylation mutations at Cx43 CT sites known to be substrates for casein kinase 1 (CK1), protein kinase C (PKC), or MAPK were subjected to pMCAO. 4 d after pMCAO, MAPK $Cx43^{S255/262/279/282A}$ (MK4) mutant mice showed several significant differences compared with WT counterparts, including a reduction in infarct volume, a decrease in apoptosis and inflammation, and an increase in astrocyte reactivity. These quantitative differences also correlated

[1]Cellular & Physiological Sciences, Life Sciences Institute, University of British Columbia, Vancouver, British Columbia, Canada; [2]Basic and Applied Medical Sciences, Ghent University, Ghent, Belgium; [3]Translational Research Program, Fred Hutchinson Cancer Research Center, Seattle, WA.

*P.D. Lampe, L. Leybaert, and C.C. Naus contributed equally to this study; Correspondence to Christian C. Naus: christian.naus@ubc.ca; Luc Leybaert: Luc.Leybaert@UGent.be.

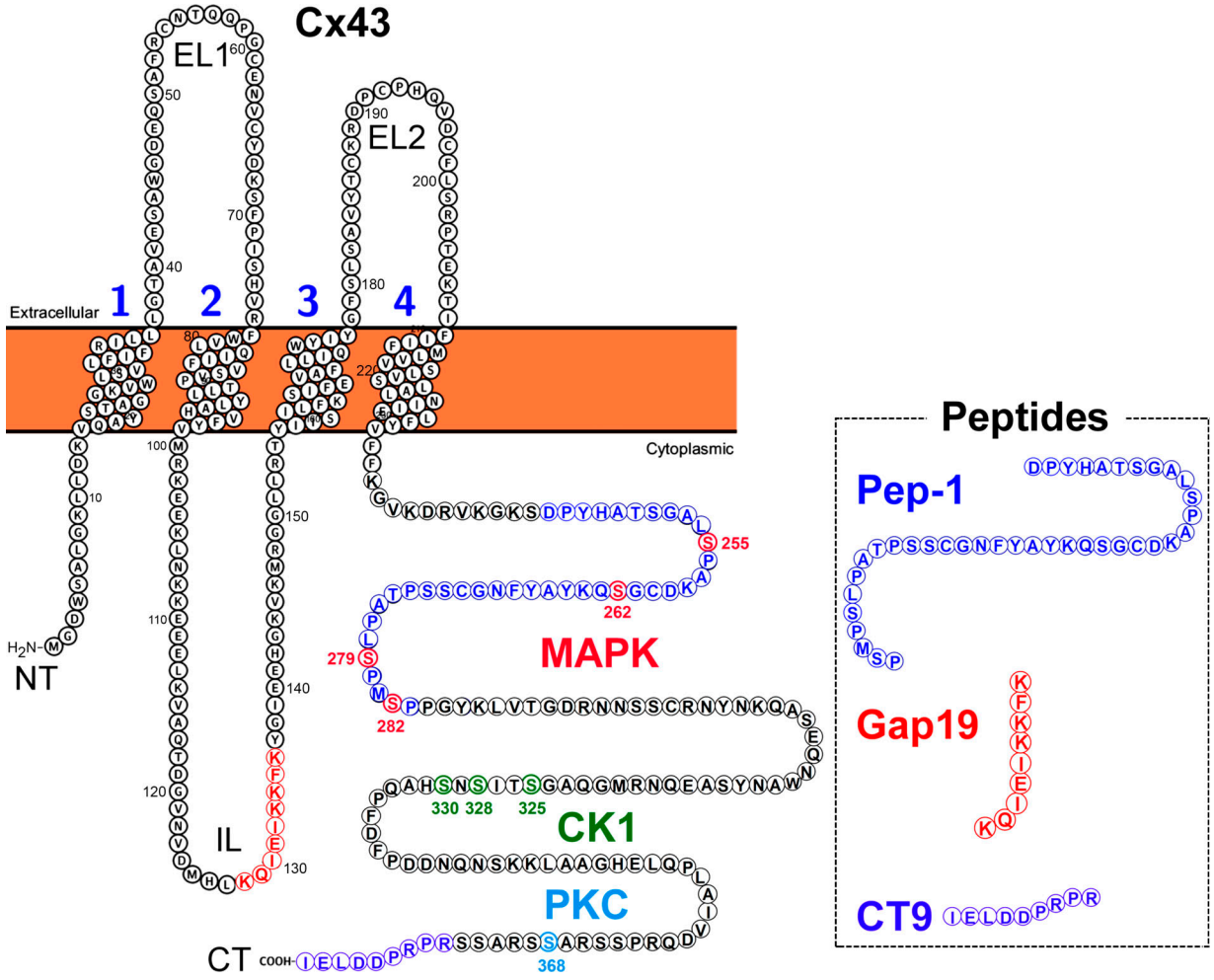

Figure 1. **Schematic indicating MAPK, CK1 and PKC phosphorylation sites on Cx43 CT domain.** Box shows peptides used in this study (sequences indicated on Cx43 protein in corresponding color). Pep-1 and CT9 fused to TAT were used for in vitro work (Fig. 6); TAT-Gap19 was used for in vivo experiments (Fig. 8). NT, N-terminal end; IL, intracellular loop; EL, extracellular loop.

with positive behavioral outcome in MK4 ischemic mice. In contrast, no significant differences in infarct volume were observed in the CK1 Cx43$^{S325A/328Y/330A}$- and PKC Cx43^{S368A}-null phosphorylation mutant animals. In addition, we demonstrate that the protective effect of the MK4 mutation during pMCAO is due to a reduction in Cx43 hemichannel activity. The mechanism was validated with the administration of the Cx43 hemichannel blocker TAT-Gap19 (Wang et al., 2013; Abudara et al., 2014) in ischemic WT mice.

Results

MK4 mice are protected following ischemic stroke

Among the known kinases that interact with Cx43 CT, CK1, PKC, and MAPK are active in ischemic conditions (Jiang et al., 2002; Freitas-Andrade et al., 2008; Kaneko et al., 2014; Demyanenko et al., 2015). To test whether disrupting CK1, PKC, or MAPK phosphorylation sites of the Cx43 C-terminal tail (Fig. 1) impacts stroke outcome, male and female WT and Cx43 phosphorylation–null mutants for CK1, PKC, and MAPK (MK4) mice were subjected to pMCAO. 4 d after pMCAO, CK1 and PKC Cx43 phosphorylation–null mutant mice did not show significant changes in infarct volume with respect to WT controls (Fig. 2, A and B). However, MK4 mice exhibited a significant ($P = 0.0181$) 58.3% reduction in infarct volume compared with their WT counterparts (Fig. 2, A and B).

In light of the compelling phenotype observed in MK4 ischemic mice, a larger cohort of WT and MK4 male and female animals were subjected to pMCAO. Consistent with our initial study, MK4 mice exhibited a significant ($P = 0.0053$) 40.2% reduction in infarct volume compared with WT counterparts (Fig. 2 C). In addition, we found no significant differences in the cortical area supplied by the middle cerebral artery (MCA) between WT and MK4 mice (data not shown).

Apoptosis triggered by an ischemic event may occur over several days and contribute to delayed neuronal death and loss of viable peri-infarct tissue (Nakase et al., 2004). To investigate whether the difference in infarct volume found in WT and MK4 ischemic mice is correlated with differences in the level of apoptosis, WT and MK4 brain sections from ischemic mice were subjected to TUNEL immunostaining. A significant ($P = 0.0322$) reduction (57.7%) in the number of apoptotic TUNEL$^+$ cells

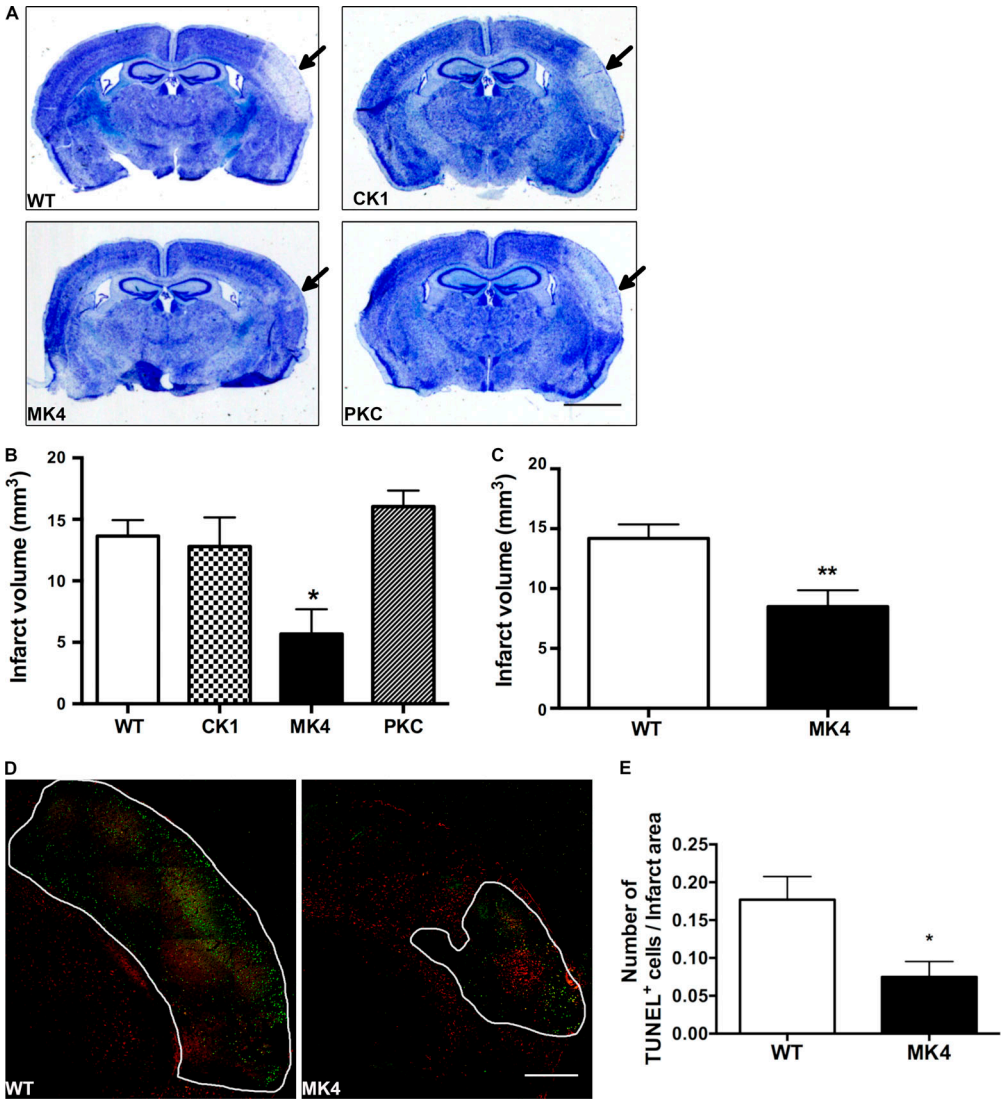

Figure 2. **Disrupting the MAPK phosphorylation sites of Cx43 CT decreases infarct volume and TUNEL staining 4 d after pMCAO. (A)** Photomicrographs of thionin-stained sections from WT and Cx43-null phosphorylation mutants CK1, PKC, and MAPK (MK4) mice 4 d after pMCAO. Arrows point to infarct region. Scale bar = 2 mm. **(B)** Quantification of infarct volume from WT and Cx43-null phosphorylation mutants CK1, PKC, and MAPK (MK4) 4 d after pMCAO (one-way ANOVA followed by Bonferroni post hoc test; *, P = 0.0181; WT: *n* = 5 mice; CK1: *n* = 4; PKC: *n* = 4; MK4: *n* = 4). **(C)** Quantification of infarct volume from WT and MK4 mice 4 d after pMCAO (unpaired Student's *t* test; **, P = 0.0053; WT: *n* = 10 mice; MK4: *n* = 11 mice). **(D)** Coimmunofluorescence staining of cerebral cortex from WT (left) and MK4 (right) mice 4 d after pMCAO using GFAP (red) with a TUNEL apoptosis marker (green). The white outline is the infarct area. Scale bar = 500 µm. Tile Scan tool and auto-stitching algorithm in the Leica LAS AF program was used to create high-resolution image montages. **(E)** Quantification of average number of TUNEL$^+$ cells in brain sections per infarct area in mm^2 from WT and MK4 mice 4 d after pMCAO (unpaired Student's *t* test; *, P = 0.0201; WT: four sections, *n* = 4 mice; MK4: four sections, *n* = 4 mice). Error bars represent mean ± SEM.

within the infarct region of MK4 sections was seen 4 d after pMCAO (Fig. 2, D and E). This was consistent with the positive thionin tissue staining within the infarct area of MK4 brain sections, indicating viable brain tissue (Fig. 2 A).

MK4 mice exhibit increased astrocyte and decreased microglia reactivity after pMCAO

Both reactive astrocytes and reactive microglia participate in stroke-induced gliosis (Burda and Sofroniew, 2014), which reaches a maximum at 3–5 d after stroke (Feuerstein et al., 1997; Nakase et al., 2004). To investigate whether MK4 mice are affected by pMCAO-induced gliosis, the total number and size of cells immunoreactive for glial fibrillary actin protein (GFAP; an astrocyte marker) and ionized calcium-binding adaptor molecule 1 (Iba1; a microglial marker) were evaluated in both WT and MK4 brain sections 4 d after pMCAO (see Fig. S1 for analysis detail).

In both WT and MK4 brain sections, an increase in the number of GFAP$^+$ cells per field of view was observed in the peri-infarct region (Fig. 3 A). However, brain sections from ischemic MK4 mice showed a significantly (P = 0.0061) larger (65.9%) increase in GFAP$^+$ cell numbers per field of view within the peri-infarct region compared with WT mice (Fig. 3, A and B). In addition, MK4 GFAP$^+$ cells were significantly (P = 0.0109)

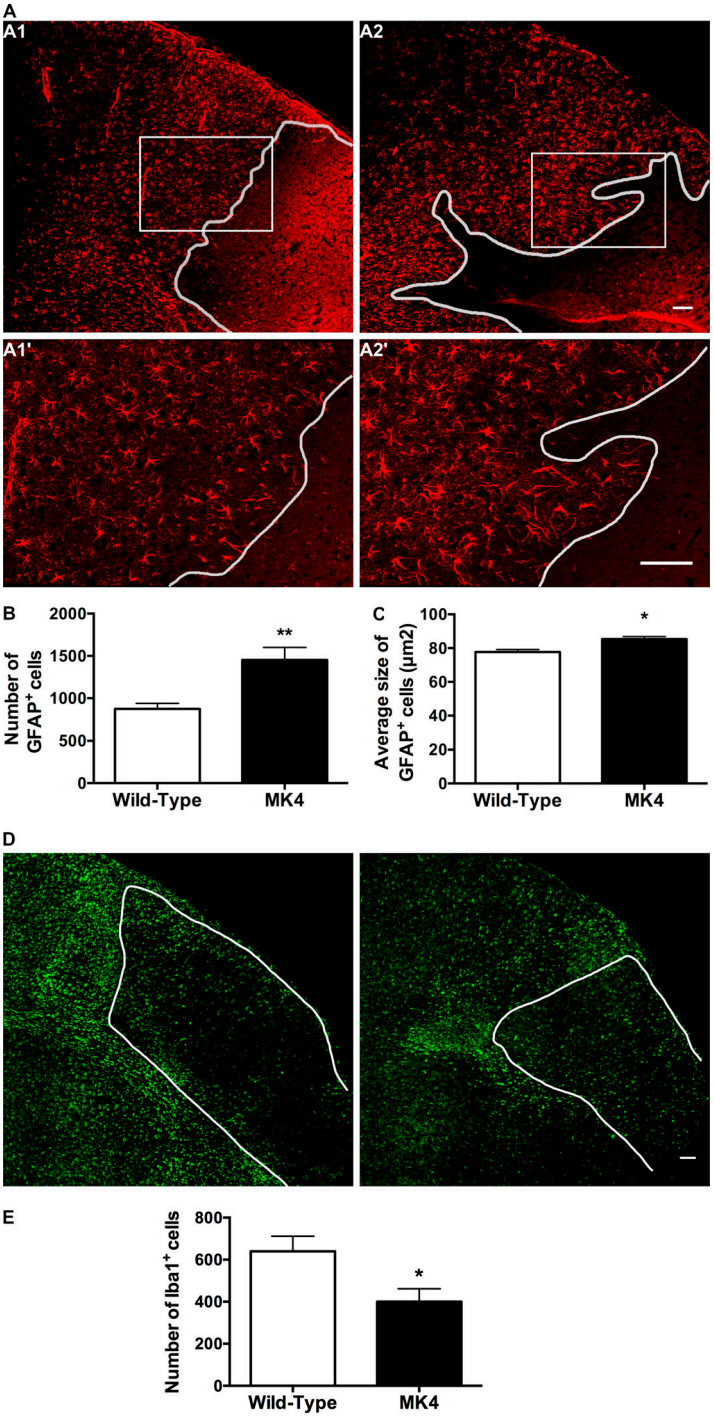

Figure 3. **Increase in GFAP⁺ reactive astrocytes and a decrease in Iba1⁺ reactive microglia 4 d after pMCAO in MK4 mice. (A)** Immunofluorescent GFAP (red) staining of WT (A1 and A1′) and MK4 (A2 and A2′) cerebral cortex from mice 4 d after pMCAO. White outlines represent the border of the infarct region. Boxes A1 and A2 (magnified in A1′ and A2′) show a larger size of individual GFAP⁺ cells in A2′ compared with A1′. **(B)** Quantification of the average number of GFAP⁺ cells per unit area (960 × 600 µm) shows a significantly higher number of GFAP⁺ cells in MK4 peri-infarct brain tissue (unpaired Student's *t* test; **, P = 0.0013; WT: four sections, *n* = 5 mice; MK4: four sections, *n* = 5 mice). **(C)** Quantification of GFAP⁺ cells reveals a significant increase in their average size in MK4 peri-infarct brain tissue (unpaired Student's *t* test; *, P = 0.0356; WT: four sections per mouse, *n* = 5 mice; MK4: four sections per mouse, *n* = 5 mice). **(D)** Immunofluorescent staining of WT (left) and MK4 (right) cortical sections 4 d after pMCAO using the microglial marker Iba1 (green). The white outline is the border of the infarct region. **(E)** Quantification of Iba1⁺ cell numbers per unit area (960 × 600 µm) shows reduction in number of Iba1⁺ cells in MK4 brain sections (unpaired Student's *t* test; *, P = 0.0211; WT: four sections per mouse, *n* = 4 mice; MK4: four sections per mouse, *n* = 4 mice). Scale bars = 100 µm. Error bars represent mean ± SEM.

larger (9.8%) than their WT counterparts (Fig. 3 A, 1′ and 2′; and Fig. 3 C). GFAP-labeled sections from MK4 mice recapitulated the thionin-staining pattern observed in Figs. 2 A and S2.

Microglia are defined partly by their morphological changes, from nonreactive small cell bodies with several thin processes to reactive microglia exhibiting a more amoeboid shape with highly branched short processes and increased Iba1 immunoreactivity (Ito et al., 2001). Iba1 immunofluorescent staining of WT and MK4 brain sections showed an increase in Iba1⁺ cells in the peri-infarct region in both genotypes (Fig. 3 D). However, MK4 sections exhibited a significant (P = 0.0448) reduction (37.4%) in Iba1⁺ cell numbers per field of view compared with WT counterparts (Fig. 3 E). No size differences in Iba1⁺ cells were observed between WT and MK4 brain sections (data not shown).

Cx43 protein expression and phosphorylation in WT and MK4 mice

We compared Cx43 spatial distribution and protein levels between WT and MK4 brain sections, 4 d after pMCAO. Immunofluorescent staining of Cx43 showed similar punctate labeling in both WT and MK4 brain sections (Fig. 4 A). In both genotypes,

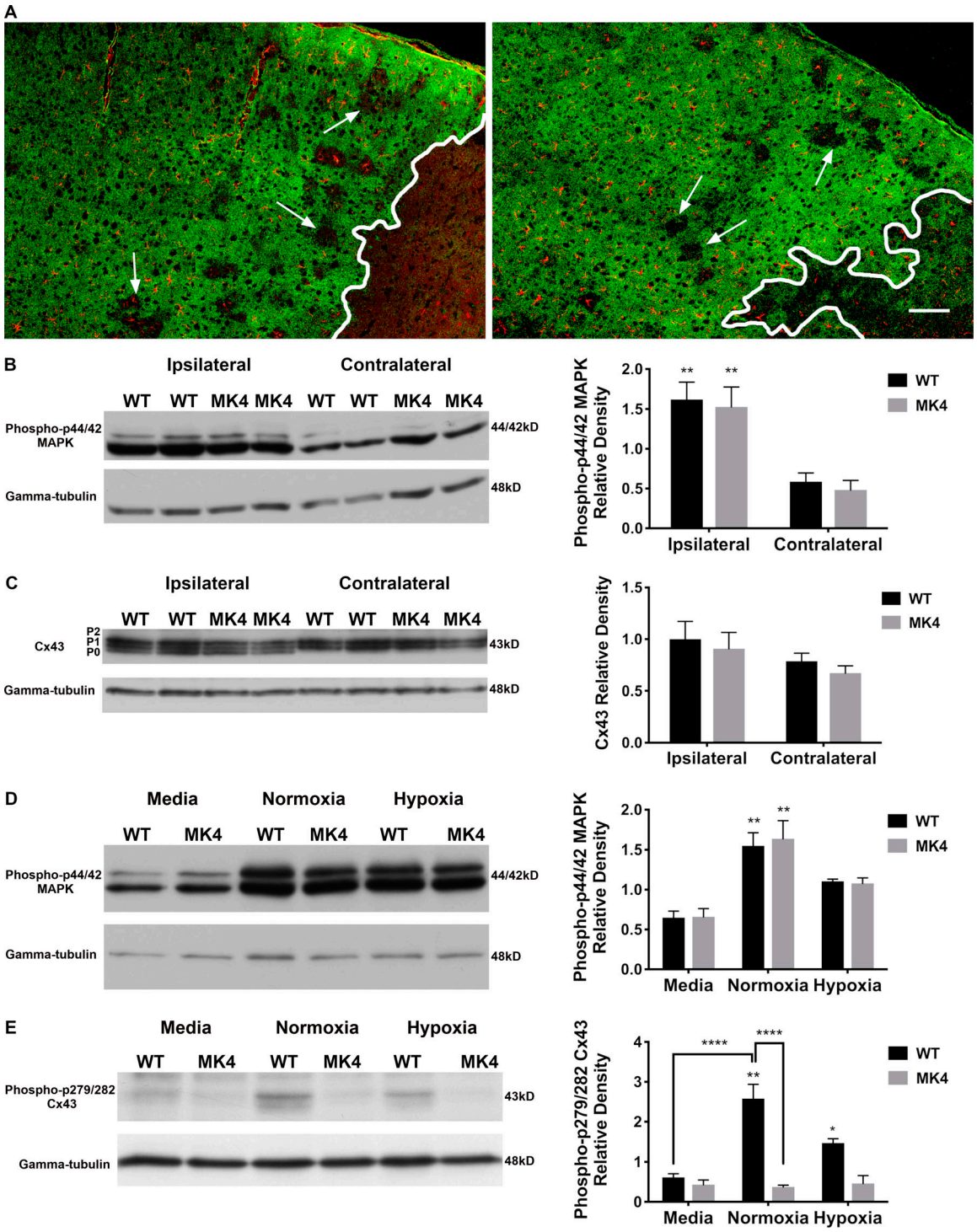

Figure 4. **Cx43 expression is similar in both WT and MK4 ischemic mice, and Cx43 phosphorylation at CT Ser sites 279 and 282 correlates with MAPK activity under ischemia. (A)** Cx43 (green) and GFAP (red) labeling in brain sections from WT (left) and MK4 (right) mice 4 d after pMCAO. Increased Cx43 staining was observed adjacent to infarct in both WT and MK4 brain sections. Arrows indicate areas within peri-infarct that did not stain for Cx43 and are devoid of GFAP signal. Infarct is indicated by the white outline. Scale bar = 100 µm. **(B)** Immunoblot of phospho-p44/42 MAPK (upper blot) and γ-tubulin (lower blot) from ipsilateral and contralateral cortical brain tissue from WT and MK4 mice 2 h after pMCAO. Right graph shows mean relative band densities for phospho-p44/42 MAPK protein as a function of side of cortex and genotype. Two-way ANOVA followed by Tukey's multiple comparisons test, main effect of genotype, P = 0.5957; main effect of treatment (ipsilateral versus contralateral cortex), ****, P < 0.0001; interaction P = 0.9724; WT ipsilateral versus WT contralateral: **, P = 0.0082; MK4 ipsilateral versus MK4 contralateral: **, P = 0.0075; WT: *n* = 4 mice; MK4: *n* = 4 mice. **(C)** Immunoblot of Cx43 (upper blot) and γ-tubulin (lower blot) from ischemic ipsilateral and nonischemic contralateral cortical brain tissue from WT and MK4 mice 2 h after pMCAO. Right graph shows mean relative band densities for Cx43 as a function of side of cortex and genotype (two-way ANOVA followed by Tukey's multiple comparisons test; no significant differences were measured between groups; WT: *n* = 4 mice; MK4: *n* = 4 mice). **(D)** Immunoblot of phospho-p44/42 MAPK (upper blot) and γ-tubulin (lower blot) in WT and MK4 astrocytes subjected to either media plus normoxia (95% O_2/5% CO_2), 3-h ischemic buffer plus normoxia (95% O_2/5% CO_2), or 3-h

ischemic buffer plus hypoxia (<1% O_2). Right graph shows mean relative band densities for phospho-p44/42 MAPK protein as a function of treatment and genotype (n = 3). Two-way ANOVA followed by Tukey's multiple comparisons test, main effect of genotype, P = 0.8297; main effect of treatment, ****, P < 0.0001; interaction P = 0.9022; WT normoxia versus WT media: **, P = 0.0038; MK4 normoxia versus MK4 media: **, P = 0.0019. **(E)** Immunoblot of phospho-p279/282 Cx43 (upper blot) and γ-tubulin (lower blot) in WT and MK4 astrocytes subjected to media, 3-h ischemic buffer plus normoxia, or 3-h ischemic buffer plus hypoxia. Right graph shows mean relative band densities for phospho-p279/282 Cx43 protein as a function of treatment and genotype (n = 3). Two-way ANOVA followed by Tukey's multiple comparisons test, main effect of genotype: ****, P < 0.0001; main effect of treatment ***, P = 0.0008; interaction, ***, P = 0.0005; WT normoxia versus WT media: ****, P < 0.0001; WT normoxia versus WT hypoxia: **, P < 0.0098; WT normoxia versus MK4 normoxia; ****, P < 0.0001; WT hypoxia versus MK4 hypoxia: *, P < 0.0204. Error bars represent mean ± SEM.

Cx43 immunoreactivity was highest adjacent to the infarct, and signal intensity decreased in proportion to the distance from the infarct (Fig. 4 A). Within the peri-infarct we observed, in both genotypes, areas where Cx43 immunostaining was not detected; these areas devoid of Cx43 also showed relatively reduced or absent GFAP signal, as indicated by white arrows (Fig. 4 A). This may represent "mini-infarct cores" surrounded by "mini-penumbras" as previously reported (del Zoppo et al., 2011). There is evidence in the literature that Cx43 is expressed in microglial cells (Eugenín et al., 2001). However, in our ischemic model, we did not detect Cx43 expression in microglia in vitro or in vivo (data not shown).

We tested whether MAPK activity is up-regulated under ischemic conditions in WT and MK4 mice 2 h after pMCAO. Consistent with previous findings (Wu et al., 2000), MAPK phosphorylation levels were significantly higher (~1.3-fold) in the ipsilateral cortex of both WT (P = 0.0082) and MK4 (P = 0.0075) animals compared with the corresponding contralateral cortex (Fig. 4 B). In both WT and MK4 mice, Cx43 protein levels were similar in the ipsilateral and contralateral cortical brain tissue 2 h after pMCAO (Fig. 4 C). However, while the contralateral tissue showed Cx43 bands corresponding to the phosphorylated P1 and P2 isoforms, the ipsilateral side showed Cx43 bands corresponding to the P0 isoform as well as the P1 and P2 isoforms in both genotypes (Fig. 4 C).

To delineate the interaction between MAPK elevated phosphorylation levels and Cx43 phosphorylation, WT and MK4 astrocytes were incubated in ischemic, high-glucose buffer (a solution that mimics the interstitial ionic concentrations of ischemic brain; Bondarenko and Chesler, 2001; Orellana et al., 2010) compared with WT and MK4 astrocytes in normal media (all at normoxia). The interaction was investigated within a 3-h timescale, which is approximately equal to the half-life of Cx43 (Laird, 1996; Saffitz et al., 2000). A significant (WT: P = 0.0038; MK4: P = 0.0019) increase (~2.5-fold) in MAPK phosphorylation levels was measured in both genotypes after 3 h in ischemic buffer in high (27 mM) glucose plus normoxia (95% O_2/5% CO_2; Fig. 4 D). However, both WT and MK4 astrocytes exposed for 3 h to ischemic buffer in high (27 mM) glucose plus hypoxia (<1% O_2) showed a nonsignificant (WT: P = 0.20; MK4: P = 0.085) trend toward higher MAPK phosphorylation compared with media controls (Fig. 4 D). In WT astrocytes, phosphorylation of Cx43 sites Ser-279 and Ser-282 correlated with MAPK activity (Fig. 4, D and E). WT astrocytes exposed for 3 h to ischemic buffer in high (27 mM) glucose plus normoxia (95% O_2/5% CO_2) exhibited a significant (P < 0.0001) increase (~4.2-fold) in phosphorylation at sites Ser-279 and Ser-282 of Cx43 compared with WT astrocytes in control media conditions (Fig. 4 E). Consistent with MAPK phosphorylation levels, WT astrocytes exposed for 3 h to ischemic buffer in high (27 mM) glucose plus hypoxia (<1% O_2) showed a nonsignificant trend toward higher phosphorylation levels at Cx43 sites Ser-279 and Ser-282 compared with media controls (Fig. 4 E). Phosphorylation of Ser-279 and Ser-282 of Cx43 was not detected in MK4 astrocytes in either condition (Fig. 4 E).

Cx43 GJ coupling is similar between ischemic WT and MK4 mice

Given that Cx43 GJ channel activity is regulated by MAPK activation (Retamal et al., 2007; Orellana et al., 2009, 2012; Kozoriz et al., 2013), Cx43 GJ coupling was evaluated in situ and in vitro in WT and MK4 astrocytes. WT and MK4 mice were subjected to pMCAO, and after 2 h of ischemia, mice were euthanized, brains were quickly removed and sliced, and tissue was scraped with a needle in a solution containing a GJ permeable dye, Lucifer Yellow (LY) and a GJ-impermeable dye, dextran rhodamine, as previously described (Desarménien et al., 2013). LY diffusion was significantly up-regulated (~2.6-fold) in the ipsilateral (ischemic) compared with the contralateral (nonischemic) cortex in both WT and MK4 mice (Fig. 5, A and B). LY diffusion in the contralateral (nonischemic) cortex was similar in both WT and MK4 brain slices (Fig. 5, A and B). 100 µM carbenoxelone (CBX), a known connexin blocker, was used to exclude the possibility that diffusion was due to an increase in cellular edema. CBX significantly blocked LY diffusion in both WT and MK4 ipsilateral cortex compared with non–CBX-treated counterparts (Fig. 5, A and B). LY diffusion was similar in both CBX-treated WT and MK4 ipsilateral and contralateral brain slices (Fig. 5, A and B).

While the in situ scrape-loading assay showed an increase in connexin-dependent LY diffusion, it is possible that other connexins, such as those expressed in neurons and/or other glial cell types, may have also contributed to LY diffusion. To investigate the role of Cx43 GJ in astrocytes specifically, an in vitro scrape-loading assay was performed in astrocytes isolated from WT and MK4 mice. Consistent with the in situ scrape-loading assay, both hypoxic WT and MK4 astrocytes demonstrated a significant (~2.5-fold) increase in GJ coupling compared with their counterpart astrocytes under control conditions (Fig. 5, C and D). No significant differences were observed between genotypes in either normoxic or hypoxic conditions (Fig. 5, C and D).

Cx43 hemichannel activity is reduced in MK4 astrocytes

To determine whether Cx43 hemichannel activity is affected in MK4 astrocytes, dye uptake assays as well as single-channel

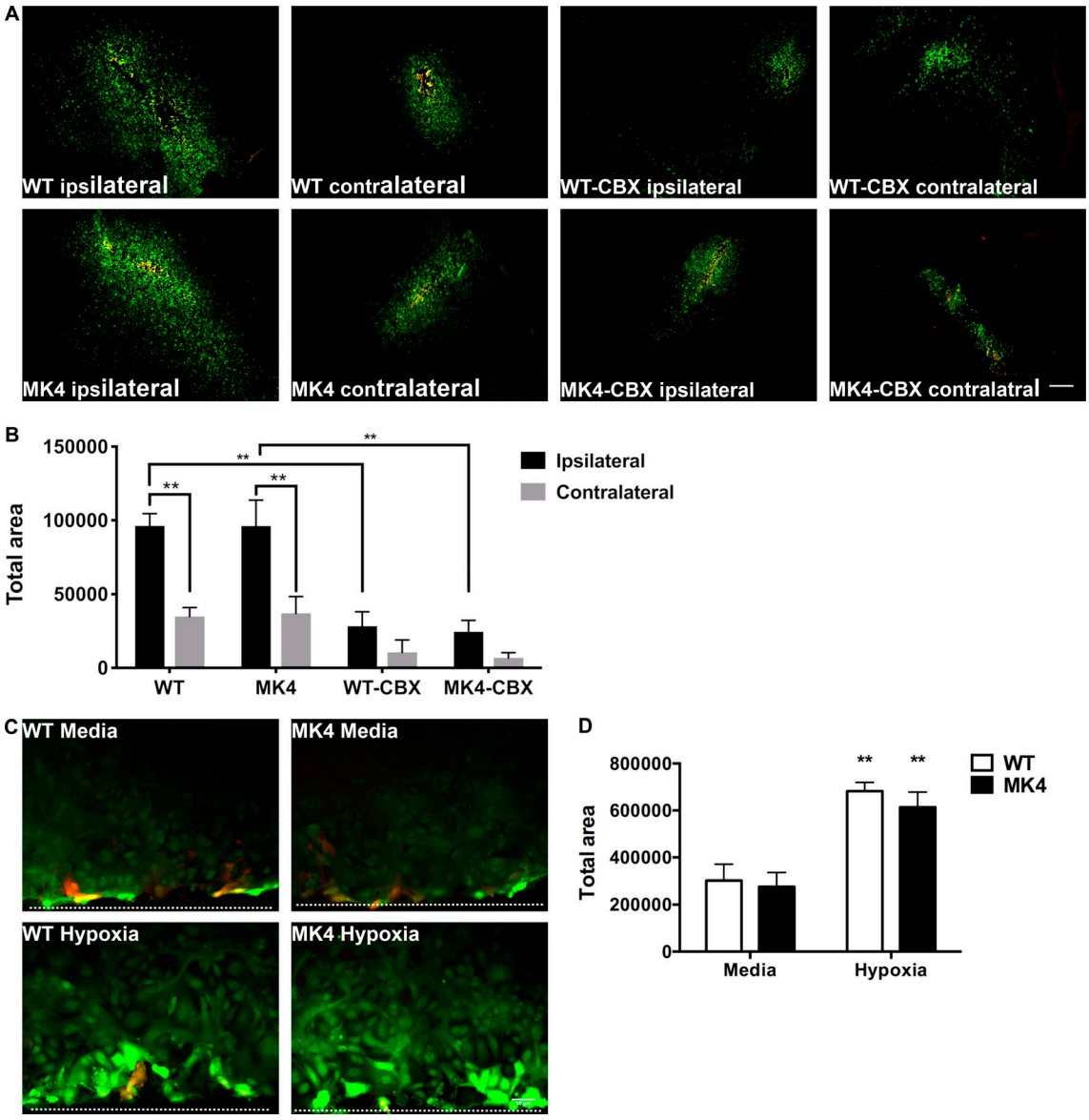

Figure 5. **Cx43 GJ coupling is similarly up-regulated in the ischemic cortex of WT and MK4 mice. (A)** In situ scrape-loading assay showing WT and MK4 ipsilateral and contralateral cortical slices incubated with the GJ-permeable dye LY (green) and the GJ-impermeable dye dextran rhodamine (red), with or without 100 µM CBX, 2 h after pMCAO. Scale bar = 200 µm. **(B)** Quantification of the total average area in LY pixels normalized to dextran rhodamine pixels in ipsilateral and contralateral brain slices from WT and MK4 mice 2 h after pMCAO. Two-way ANOVA followed by Tukey's post hoc test, main effect of genotype/treatment: ****, $P < 0.0001$; main effect of brain region (ipsilateral/contralateral), ****, $P < 0.0001$; interaction, $P = 0.1148$, WT: $n = 5$ mice; MK4: $n = 5$ mice; WT-CBX treated: $n = 3$ mice; MK4-CBX treated $n = 3$. WT ipsilateral versus WT contralateral, **, $P = 0.0053$; MK4 ipsilateral versus MK4 contralateral, **, $P = 0.0078$; WT-CBX ipsilateral versus WT ipsilateral **, $P = 0.0081$; MK4-CBX ipsilateral versus MK4 ipsilateral **, $P = 0.0048$. **(C)** In vitro scrape-loading assay (dotted line shows scrape edge) showing WT and MK4 astrocytes exposed to either media plus normoxia (95% O_2/5% CO_2) or 3-h ischemic buffer plus hypoxia (<1% O_2) incubated with LY (green) and dextran rhodamine (red). Scale bar = 50 µm. **(D)** Quantification of total average diffusion area in LY pixels normalized to dextran rhodamine pixels in WT and MK4 astrocytes subjected to either media plus normoxia (95% O_2/5% CO_2) or 3-h ischemic buffer plus hypoxia (<1% O_2). Two-way ANOVA followed by Tukey's post hoc test, main effect of genotype, $P = 0.2985$; main effect of treatment, ****, $P < 0.0001$; interaction, $P = 0.6338$, WT hypoxia versus WT media: **, $P = 0.0049$; MK4 hypoxia versus MK4 media: **, $P = 0.0015$; $n = 4$. Error bars represent mean ± SEM.

recordings were performed and compared between WT and MK4 astrocytes. Decreasing extracellular divalent cations is a well-known stimulus for hemichannel opening; in line with this, we found that applying Ca^{2+}- and Mg^{2+}-free solutions triggered ethidium uptake in WT astrocytes (Fig. 6 A). Interestingly, ethidium uptake was significantly less in astrocytes from MK4 animals, indicating decreased hemichannel function (WT slope = 42.16 ± 0.3281; MK4 slope = 25.30 ± 0.1738; $n = 3$). We next tested ethidium uptake under conditions of 3-h hypoxia followed by 1-h reoxygenation, which is known to increase hemichannel activity and decrease GJ coupling in cortical astrocytes (Orellana et al., 2010). Consistently, we found that ischemic conditions triggered ethidium uptake in WT astrocytes (Fig. 6 B), while uptake was significantly lower in MK4 astrocytes (WT slope = 42.98 ± 0.8610; MK4 slope = 31.96 ± 0.5885; $n = 6$).

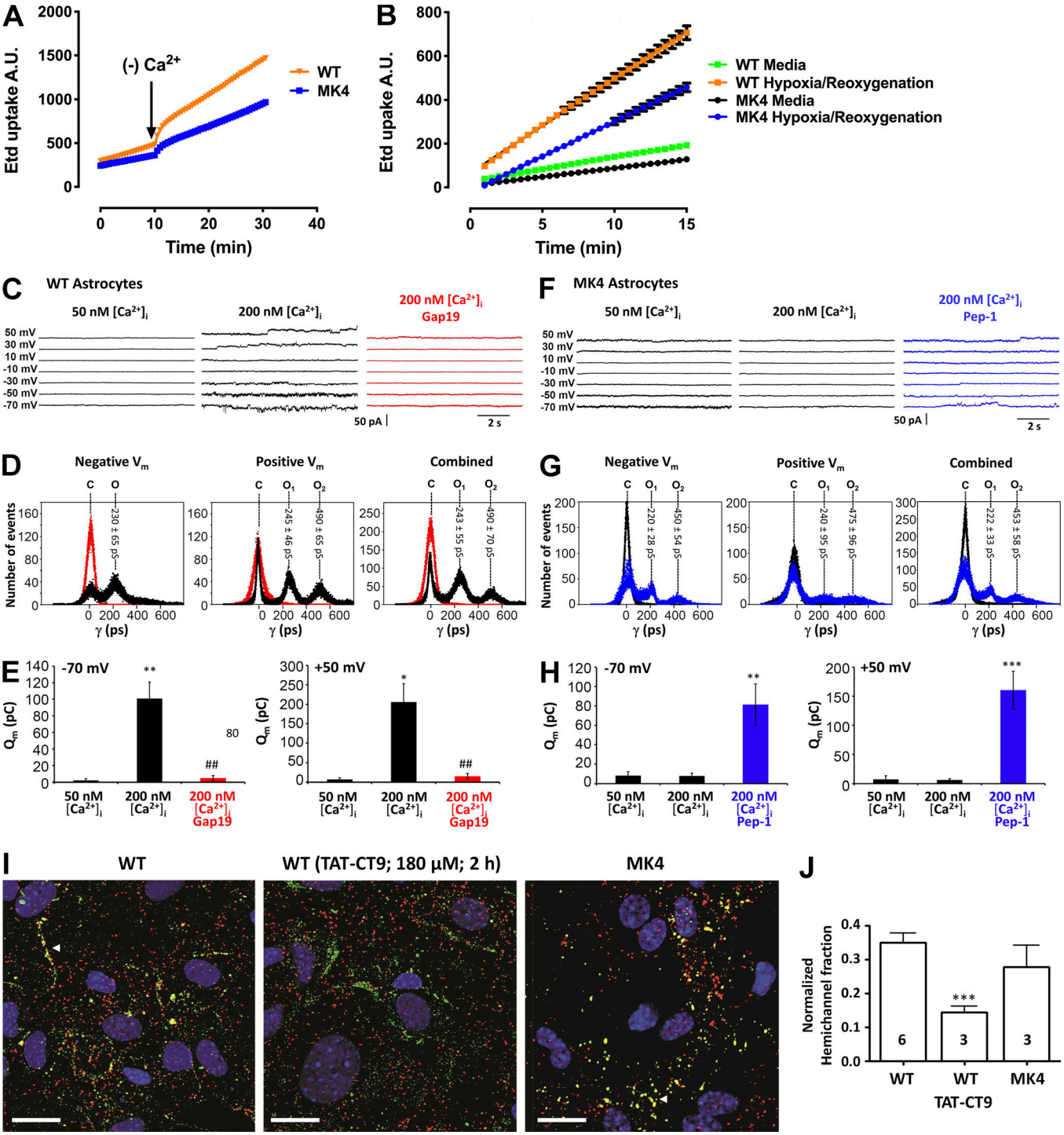

Figure 6. **Hemichannel activity is reduced in MK4 astrocytes. (A)** Time-lapse measurements of ethidium uptake in WT or MK4 astrocytes exposed to 5 µM EtBr. At 10 min, solution was changed to Ca^{2+}/Mg^{2+}-free solution (divalent free) to induce hemichannel opening. Linear regression performed in WT and MK4 reveals slopes are significantly different (n = 3; ****, $P < 0.0001$). **(B)** Time-lapse measurements of ethidium uptake in WT and MK4 astrocytes under normoxic conditions (green and black lines, respectively) or 3-h hypoxia in ischemic buffer followed by 1-h reoxygenation in media (orange and blue lines, respectively). After treatment, astrocytes were exposed to 5 µM EtBr for 15 min. Linear regression was performed in WT and MK4 hypoxia/reoxygenation–treated samples; slopes are significantly different (n = 6; **, $P < 0.001$). **(C–E)** Patch-clamp studies of hemichannel activity. **(C)** Current traces in WT astrocytes for voltage steps indicated on the left. Unitary current activity appeared at both negative and positive V_m when $[Ca^{2+}]_i$ was elevated from 50 nM to 200 nM. Gap19 (100 µM, added via pipette) suppressed unitary activity (red traces). **(D)** All-point histogram of current activities at negative, positive, and combined V_m. Unitary conductance of one (O_1) or two open hemichannels (O_2) are indicated above each peak (mean ± SD). Gap19 abolished all current activity (red peak at baseline). **(E)** Charge transfer (Q_m) associated with unitary current activities for recordings at −70 and +50 mV (n = 6). *, $P < 0.05$ versus 50 nM $[Ca^{2+}]_i$; **, $P < 0.01$; ##, $P < 0.01$ versus 200 nM $[Ca^{2+}]_i$. **(F)** Current traces in MK4 astrocytes. Unitary activity was absent at 200 nM $[Ca^{2+}]_I$, but pretreatment with 35 µM Pep-1 peptide (1 h) restored activity (blue traces). **(G)** All-point histogram showing that currents restored by Pep-1 had a single-channel conductance similar to WT. **(H)** Q_m

charge transfer data illustrating restoration of opening activities with Pep-1 in MK4 astrocytes (n = 6). **, P < 0.01 compared with 200 nM $[Ca^{2+}]_i$; ***, P < 0.001. **(I)** Confocal images of Duolink (red) and Cx43 (green) stainings in WT and MK4 astrocytes; yellow colocalization signal corresponds to hemichannels. WT astrocytes (left) displayed clear hemichannel signal (arrowhead) that was decreased after TAT-CT9 treatment; hemichannel signal was also present in MK4 astrocytes (right). **(J)** Summary data of normalized yellow signal, demonstrating that the MK4 signal was not different from WT. ***, P < 0.001 WT versus WT (TAT-CT9). Scale bars = 20 µm. Error bars represent mean ± SEM.

We further investigated Cx43 hemichannel properties, making use of whole-cell patch-clamp experiments in primary cultured astrocytes. In WT astrocytes, no unitary current activities were observed at 50 nM $[Ca^{2+}]_i$ (applied through the pipette), even with voltage steps up to +50 mV. By contrast, increasing $[Ca^{2+}]_i$ to 200 nM provoked unitary currents over a wide range of positive as well as negative potentials (Fig. 6 C). All-point histograms for negative and positive membrane potentials (Fig. 6 D) demonstrated a unitary conductance in the range of 230–245 pS (i.e., close to the approximate value of 220 pS reported for Cx43 hemichannels; Contreras et al., 2003; Wang et al., 2012). Gap19, a nonapeptide derived from the cytoplasmic loop of Cx43 (Fig. 1) and previously shown to inhibit hemichannel activity without inhibiting GJ coupling (Wang et al., 2013; Abudara et al., 2014), abolished the unitary current activities (Fig. 6 C). Fig. 6 E summarizes membrane charge transfer data, which was negligible at 50 nM $[Ca^{2+}]_i$ while significantly enhanced at 200 nM $[Ca^{2+}]_i$ and reduced to baseline by Gap19 added via the recording pipette (Fig. 6 E). As predicted by the dye-uptake experiments, electrical and chemical (200 nM $[Ca^{2+}]_i$) stimulation did not trigger any hemichannel current activity in MK4 astrocytes (Fig. 6 F). We next tested whether supplying MK4 astrocytes with a cell-penetrating peptide called Pep-1, composed of Asp-245 to Pro-283 on the Cx43 CT encompassing the four Ser residues modified in MK4 mice (Fig. 1), could rescue hemichannel activity. Strikingly, preincubating MK4 astrocytes with Pep-1 rescued hemichannel activities in MK4 astrocytes at 200 nM $[Ca^{2+}]_i$ (Fig. 6 F), which had a unitary conductance of 220–240 pS (Fig. 6 G; i.e., not different from those in WT astrocytes) and were associated with significantly increased charge transfer as compared with nontreated astrocytes (Fig. 6 H).

To exclude the possibility that the lower unitary hemichannel activity is due to a smaller pool of plasma membrane hemichannels in MK4 astrocytes, we performed Duolink in situ proximity ligation assays in isolated WT and MK4 astrocytes. This assay reports the spatial hemichannel organization relative to GJs through amplification of Cx43–ZO-1 complexes that represent hemichannels (Rhett et al., 2011). As illustrated in Fig. 6 I, red Duolink fluorescence occurred throughout the cells, while the yellow signal produced by red-green colocalized spots at GJs (arrowhead) represents hemichannels in the "perinexus" (i.e., closely associated with GJs; Palatinus et al., 2012). We further tested TAT-CT9, a peptide composed of the last nine amino acids of the Cx43 C-terminal end (Fig. 1) fused to the TAT (transactivator of transcription) membrane translocation sequence; this peptide promotes incorporation of hemichannels into GJs by competing for ZO-1 binding, for which the four last amino acids of the C-terminal tail are crucial (Jin et al., 2004). WT astrocytes treated with 180 µM TAT-CT9 (2 h) displayed markedly less Duolink fluorescence signal, in line with its promoting effect on hemichannel assembly into GJs (Fig. 6 I). Quantification of the yellow signal relative to the green Cx43 signal corresponding to the normalized plasma membrane hemichannel fraction showed that the signal in MK4 astrocytes was not different from the signal in WT cells (Fig. 6 J). Thus, the lower hemichannel activity in MK4 astrocytes is the consequence of altered gating and not the result of a decreased hemichannel pool.

Functional deficit is reduced in MK4 mice subjected to pMCAO

To determine whether the significant reduction in infarct volume measured in MK4 mice is correlated with reduced functional deficits, ischemic WT and Cx43 MK4 mice were subjected to the adhesive tape removal test. In WT mice, pMCAO significantly increased the time it took for mice to remove tape from the left (impaired) paw 3 d after surgery (WT = 39.78 ± 54.90 s versus MK4 = 7.33 ± 4.30 s; P = 0.0345; Fig. 7 A). In addition, 5 and 9 d after surgery, WT mice exhibited a nonsignificant latency in tape removal compared with MK4 animals (Fig. 7 A). By 14 and 21 d after pMCAO, WT mice became as efficient on the tape removal test as their MK4 counterparts (Fig. 7 A). For the right (nonimpaired) forepaw, there was no significant effect of pMCAO on tape removal latency between the two genotypes (Fig. 7 B).

At the end of the adhesive tape removal experiment (21 d of recovery from pMCAO), infarct damage was assessed in both WT and MK4 mice by thionin staining of brain sections (Fig. 7 C). Fibrotic scar tissue was evident by intense thionin staining on both WT and MK4 brain sections (Fig. 7 C). This was also confirmed by intense $GFAP^+$ immunofluorescent staining, within the glial limitans, indicating formation of glial scar (Burda and Sofroniew, 2014; Fig. 7 F). Fibrotic scar tissue volume was increased in thionin-stained brain sections, and a significant (P = 0.0338) 40.0% reduction in scar tissue volume was measured in brain sections from MK4 mice compared with WT animals (Fig. 7 D). In thionin-stained sections, cortical loss in the ipsilateral infarct side with respect to the contralateral side was evident in both WT and Cx43 MK4 mice (Fig. 7 C). Quantification of percent brain loss showed no significant difference in cortical loss in MK4 ipsilateral cortex compared with WT counterparts (Fig. 7 E). The ipsilateral stroke area showed a significant decrease in cortical thickness in both WT and MK4 animals compared with contralateral cortex; however, no significant difference between the two genotypes was found (Fig. S3).

WT and MK4 brain sections from mice 21 d after pMCAO were labeled with GFAP and Cx43 antibodies. In both WT and MK4 mice, intense $GFAP^+$ and $Cx43^+$ staining was observed in the infarct tissue (Fig. 7 F). Cx43 expression was increased in $GFAP^+$ cells, particularly within the glial limitans surrounding

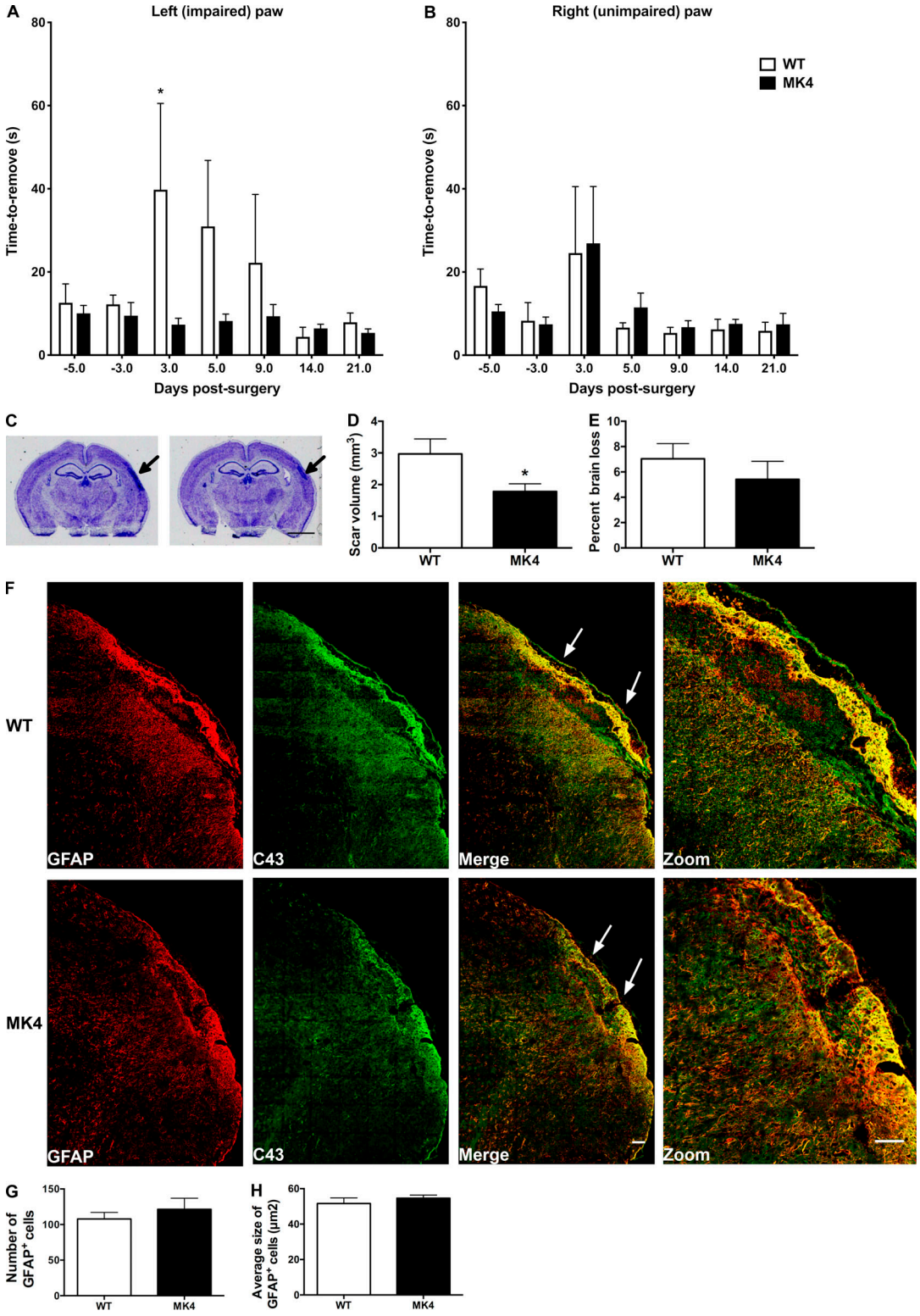

Figure 7. **MK4 mice show improved sensory function and decreased fibrotic scar tissue after pMCAO. (A)** Quantification of average time to remove adhesive tape from left (impaired) forepaw. Times −5 and −3 represent days prior to pMCAO. **(B)** Latencies for right forepaw were unaffected by pMCAO. Two-way ANOVA with repeated measures followed by Bonferroni's multiple comparisons test, main effect of genotype, P = 0.1200; main effect of time, P = 0.1178; subjects (matching), **, P = 0.0027; interaction, P = 0.1534. The observed power for the interactions is 0.588. The effect size of interaction between time and genotype is 0.3, according to Cohen's f (medium to large effect). WT mice versus MK4 mice 3 d after pMCAO: *, P = 0.0345; WT: *n* = 7 mice; MK4: *n* = 8 mice. **(C)** Thionin-stained sections from WT and MK4 mice 21 d after pMCAO. Arrows indicate fibrotic scar. Scale bar = 2 mm. **(D)** Quantification of scar volume from WT and MK4 thionin-stained sections (unpaired Student's *t* test; *, P = 0.0338; WT: *n* = 6 mice; MK4: *n* = 8 mice). **(E)** Quantification of cortical percent loss with respect to contralateral cortex between WT and MK4 mice 21 d post-pMCAO (unpaired Student's *t* test; P = 0.4221). **(F)** Example images of GFAP (red) and

Cx43 (green) labeled brain sections from WT and MK4 mice 21 d after pMCAO. Images on the far right are expanded (2× optical zoom) views of the scar tissue in the micrographs shown on the left. White arrows indicate scar tissue. Scale bar = 100 µm. The Tile Scan tool and autostitching algorithm in the Leica LAS AF program was used to create high-resolution image montages. **(G)** Quantification of average number of GFAP$^+$ cells in WT and MK4 mice (unpaired Student's *t* test; P = 0.5215; WT: four sections per mouse, *n* = 5 mice; MK4: four sections per mouse, *n* = 5 mice). **(H)** Quantification of average size of astrocytes in WT and MK4 mice (unpaired Student's *t* test; P = 0.3852; WT: four sections per mouse, *n* = 5 mice; MK4: four sections per mouse, *n* = 5 mice). Error bars represent mean ± SEM.

the scar tissue (Fig. 7 F). Quantification of GFAP$^+$ cell numbers and size showed no significant difference between the two genotypes (Fig. 7, G and H). Within the fibrotic scar tissue, large amounts of cellular debris and/or extracellular matrix protein were observed that resulted in nonspecific staining (Fig. 7 F, zoom).

Blocking Cx43 hemichannel activity is neuroprotective in mice subjected to pMCAO

We next asked whether the decreased hemichannel activity exhibited in MK4 astrocytes is a key factor in the neuroprotective phenotype of these animals subjected to pMCAO. We subjected WT animals to pMCAO followed by pharmacological administration of either the hemichannel blocker TAT-Gap19 (Abudara et al., 2014) or its scrambled form, TAT-GAP19-scrambled. Fusion of Gap19 to the TAT sequence facilitates cellular uptake of the peptide, allowing it to cross the blood–brain barrier (BBB) after intracarotid injection (Wang et al., 2013; Abudara et al., 2014). We tested whether i.p. injection of 7.5 µmol/kg Biotin-TAT-Gap19 sufficiently crossed the BBB and was detectable in the brain parenchyma. 10 min after i.p. injection, Biotin-TAT-Gap19 was detected at the level of the basal lamina around blood vessels, and at 80 min, it was present in GFAP-positive astrocytes, where it colocalized with Cx43 (Fig. S4).

After 2 h of pMCAO, i.p. injection of either 0.75 µmol/kg or 7.5 µmol/kg TAT-Gap19 significantly reduced infarct volume by 47.8% and 77.6%, respectively, 4 d after pMCAO compared with those mice that received saline or scrambled peptide alone (Fig. 8, A and B). Mice treated with the negative control TAT-Gap19-scrambled did not show significant changes with respect to saline controls (Fig. 8, A and B). Mice treated with 7.5 µmol/kg TAT-Gap19 showed a significant reduction in infarct volume compared with mice treated with 0.75 µmol/kg of TAT-Gap19 (Fig. 8 B).

Discussion

Kinase activity is induced by a plethora of stimuli triggered by stroke. Cx43 phosphorylation by PKC has been reported to preferentially occur in the cerebellum (Márquez-Rosado et al., 2012), an area of the brain that is not affected by our pMCAO model. In addition, while we show an increase in Cx43 expression levels in the peri-infarct area 4 d after pMCAO, PKC expression has been shown to spike during the onset of ischemia but quickly disappears within the peri-infarct zone at later time points (Cui et al., 2011; Lucke-Wold et al., 2015). Similarly, in rats subjected to global ischemia, CK1 activity is down-regulated in vulnerable hippocampal CA1 neurons (Kaneko et al., 2014). Therefore, the difference in spatial and/or temporal overlap between CK1 and PKC with respect to Cx43 expression may explain the lack of effect on infarct volume as observed here. Alternatively, a plausible explanation could be that phosphorylation of Cx43 by different kinases, triggered by ischemia, may induce compensatory overlapping responses associated with PKC and CK1 with regard to Cx43 channels (Pogoda et al., 2016). These results do not exclude the possibility that PKC or CK1 may act on Cx43 in other brain pathologies.

In both WT and MK4 ipsilateral cortex, MAPK phosphorylation was increased compared with the contralateral side 2 h after pMCAO, in agreement with previous findings (Wu et al., 2000). Similarly, MAPK phosphorylation levels were more pronounced in both WT and MK4 astrocytes when stressed for 3 h in ischemic buffer in vitro, which was directly correlated with an increase in phosphorylation levels in Ser-279/282 of Cx43 in WT astrocytes. These findings are further supported by a recent study showing that Cx43 phosphorylation is up-regulated as early as 2 h and as late as 8 h after bilateral common carotid occlusion in rats and that Cx43 phosphorylation is blocked by inhibiting MAPK activity (Chen et al., 2017). We show here that Cx43 phosphorylation at Ser-279/282 was also detected 24 h after pMCAO (Fig. S5 B).

While several lines of evidence indicate that MAPK-dependent phosphorylation of Cx43 decreases GJ coupling (Warn-Cramer et al., 1998; Sirnes et al., 2009; Nimlamool et al., 2015), the level of GJ coupling in WT astrocytes was similar to that seen in MK4 astrocytes after 2 h of pMCAO in vivo or 3 h of exposure to ischemic conditions in vitro. Although our data did not support a role for MAPK-dependent disruption of GJ coupling in ischemic WT astrocytes, this does not exclude the possibility that MAPK-dependent reduction of GJ coupling may have occurred more robustly at a different time point than the 2 and 3 h explored in this study. We detected changes in Cx43 phosphorylation, based on electrophoretic isoforms analyzed by immunoblot, in the ipsilateral cortex compared with the corresponding contralateral side in both genotypes 2 h after pMCAO. The faster-migrating P0 isoform detected in both WT and MK4 ipsilateral cortex is not phosphorylated at MAPK sites on Cx43 (Solan and Lampe, 2009). Interestingly, evidence in the literature indicates that some phosphorylated species migrate with the P0 band in SDS-PAGE (Solan and Lampe, 2009). Therefore, one cannot exclude the possibility that the P0 isoform is phosphorylated at some other site. It has been shown that the P0 isoform is associated with increased coupling in ischemic astrocytes in vivo (Li et al., 1998). Others have reported a link between GJ coupling and increased astrocyte reactivity in brain injury (Naus et al., 2001; Siushansian et al., 2001; Ozog et al., 2002; Nakase et al., 2003; Wallraff et al., 2006; Belousov et al.,

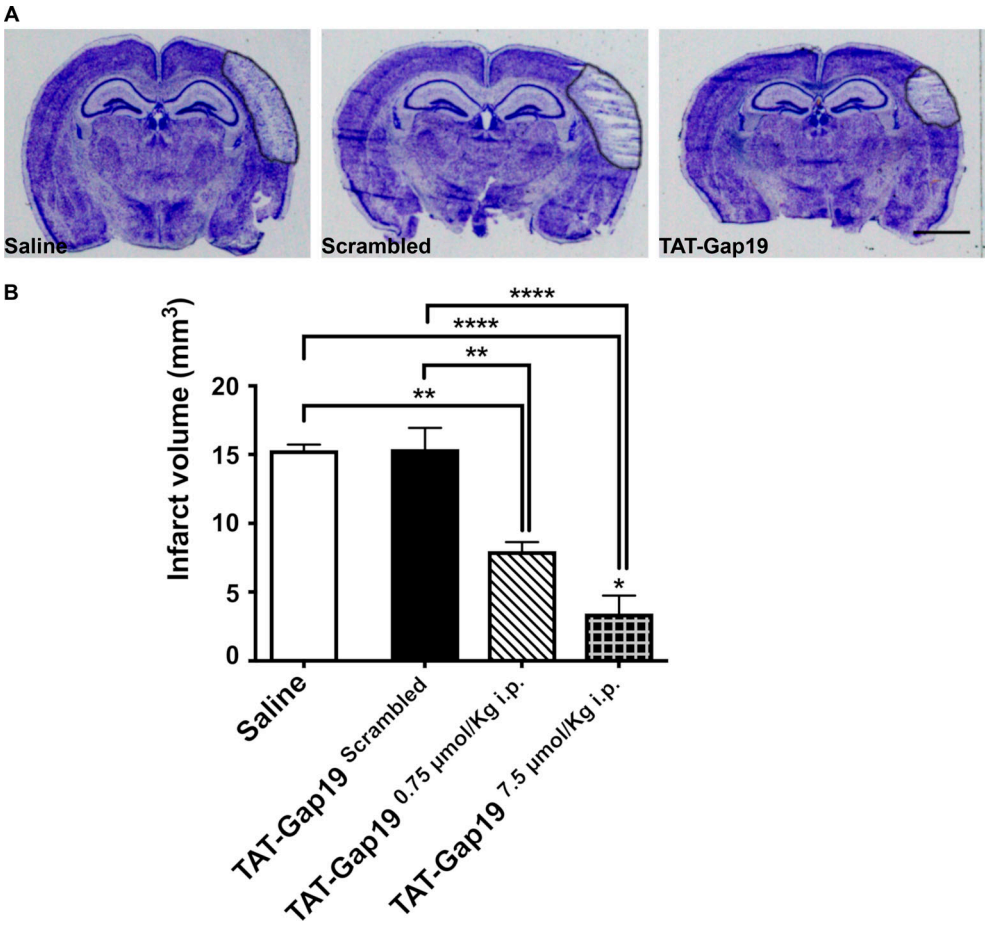

Figure 8. **TAT-Gap19 is neuroprotective in mice subjected to pMCAO. (A)** Thionin-stained sections 4 d after pMCAO in WT mice treated with saline, 7.5 µmol/kg i.p. scrambled TAT-GAP19-scrambled, or 0.75 µmol/kg i.p. hemichannel blocker TAT-GAP19 2 h after pMCAO. Black outline highlights the infarct. Scale bar = 2 mm. **(B)** Infarct volume 4 d after pMCAO from WT mice treated with saline, TAT-GAP19-scrambled, or TAT-GAP19 2 h after pMCAO (one-way ANOVA followed by Tukey's multiple comparisons test; saline versus scrambled: P > 0.9999; saline versus 0.75 µmol/kg TAT-GAP19: **, P = 0.0021; saline versus 7.5 µmol/kg TAT-GAP19: ****, P = < 0.0001; scrambled versus 0.75 µmol/kg TAT-GAP19: **, P = 0.0019; scrambled versus 7.5 µmol/kg TAT-GAP19: ****, P < 0.0001; 0.75 µmol/kg TAT-GAP19 versus 7.5 µmol/kg TAT-GAP19: *, P = 0.0484; saline: *n* = 4 mice; 7.5 µmol/kg TAT-GAP19-scrambled: *n* = 4 mice; 7.5 µmol/kg TAT-GAP19: *n* = 4 mice; 0.75 µmol/kg TAT-GAP19: *n* = 4). Error bars represent mean ± SEM.

2017). Interestingly, a marked increase in GFAP$^+$ astrocyte size and cell numbers in MK4 mice compared with WT counterparts was measured. We postulate that Cx43 in both MK4 and WT mice was subjected to the same ischemia-dependent dephosphorylation. However, due to the additional insensitivity of Cx43 to MAPK phosphorylation in MK4 mice, this may have contributed to prolonged Cx43 GJ coupling and increased astrocyte reactivity within the 4 d of pMCAO. Several lines of evidence show that reactive astrocytes are involved in neuronal survival mechanisms in stroke and neurodegeneration (Li et al., 2008; Kraft et al., 2013; Kamphuis et al., 2015). Therefore, the increased astrocyte reactivity in MK4 mice, measured 4 d after stroke, may have contributed to the significantly smaller infarct volumes observed in these animals as well as the reduced fibrotic scar at 21 d after stroke.

Previous reports have shown that Cx43 hemichannel activity under in vitro pathological conditions is linked with inflammation and neuronal death (Retamal et al., 2007; Froger et al., 2010; Orellana et al., 2010, 2011). In agreement with these reports, the reduced levels of Cx43 hemichannel activity exhibited by MK4 mice is correlated with a reduction in the number of Iba1$^+$ microglial and TUNEL$^+$ apoptotic cells 4 d after pMCAO. These findings, together with other studies, suggest that reduced hemichannel activity may provide a protective microenvironment that enables both astrocyte and neuronal survival after stroke in MK4 animals.

The Duolink assays and immunoblot experiments confirmed that the differences in hemichannel activity exhibited between WT and MK4 astrocytes were not due to differences in Cx43 protein levels or hemichannel pool alterations. Furthermore, electrophysiological evidence demonstrated that Pep-1 peptide encompassing the WT C-terminal MAPK phosphorylation sites (Fig. 1) rescued deficient hemichannel activity in MK4 astrocytes, indicating that Ser-255, Ser-262, Ser-279, and Ser-282 are crucial for hemichannel function. The hemichannel-inhibiting peptide Gap19 acts by binding to the C-terminal tail, thereby preventing intramolecular loop–tail interactions that are necessary for hemichannels to become available for opening

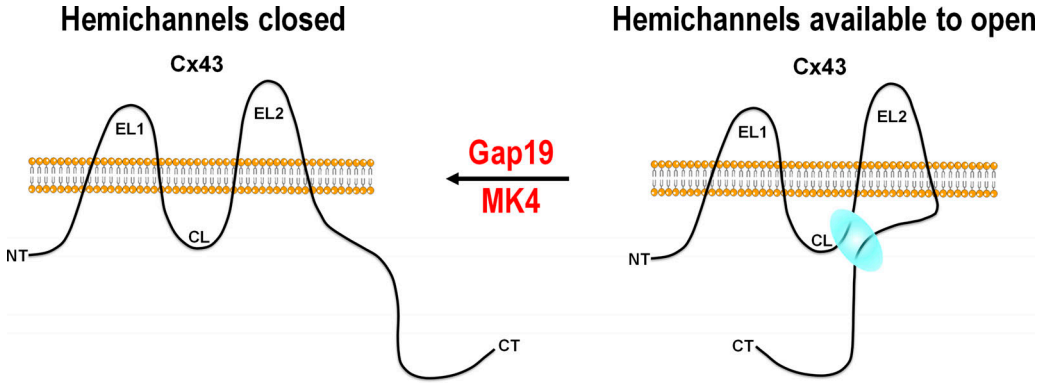

Figure 9. **Model for MAPK consensus Ser phosphorylation sites in loop–tail interaction and regulation of Cx43 hemichannel function.** Interaction of CL with MAPK consensus phosphorylation site encompassing Ser-255, Ser-262, Ser-279, and Ser-282 on the CT (blue interaction cloud) brings hemichannels into a state available for opening. Modification of the four Ser residues to Ala in MK4 animals prevents loop–tail interaction and therefore prevents hemichannel opening. Gap19 prevents hemichannel opening by binding to the CT, thereby hindering loop–tail interaction. NT, N-terminal end; EL, extracellular loop; CL, cytoplasmic loop.

(Ponsaerts et al., 2010; Wang et al., 2013; Fig. 9). In line with deficient loop–tail interaction in MK4 animals, we recently found that Ser-279 and Ser-282, in addition to the last nine amino acids of the C-terminal end (Arg-374–Ile-382, marked purple in Fig. 1), are crucial for hemichannel function (Iyyathurai et al., 2018). The Ser-279/Ser-282–containing domain (called the Src homology 3 or SH3 domain, Pro-274–Pro-284) and the CT9 domain appear to be involved, with modifications in one of these domains giving diminished Cx43 hemichannel activity and modifications in both resulting in complete hemichannel block. The present data indicate that Ser to Ala modification in the longer His-248–Lys-287 stretch, containing Ser-255, Ser-262, Ser-279, and Ser-282, produces almost complete loss of hemichannel function, thereby protecting the brain. The data presented here suggest that phosphorylation on one or more of the MAPK consensus Ser phosphorylation sites may play a role in the loop–tail interaction.

Taken together, the data highlight MAPK as a player in ischemic damage within the context of Cx43 function. Interestingly, this intracellular kinase has been reported to exhibit both beneficial and detrimental effects that may be context dependent (i.e., cell type or temporal activation of MAPK; Sawe et al., 2008). Indeed, several reports have demonstrated that MAPK inhibition is beneficial in stroke (reviewed in Sun and Nan, 2016). This is consistent with the beneficial effect of inhibiting or disrupting MAPK phosphorylation of Cx43 in ischemic conditions.

Several studies with nonspecific GJ/hemichannel blockers such as halothane, octanol, and CBX have demonstrated protective effects on infarct size or cell death in various permanent or transient animal stroke models (Warner et al., 1995; Rawanduzy et al., 1997; Saito et al., 1997; Rami et al., 2001; de Pina-Benabou et al., 2005; Perez Velazquez et al., 2006). Work with more specific connexin mimetic peptides like Gap26 or Gap27, which first block hemichannels and, with some delay, GJs, also reduced infarct size and cell death, and promoted functional recovery, even if added 24 h after ischemia. The effect was explained by alterations in the trafficking and degradation of Cx43 and reduced extracellular glutamate but hemichannel function was not tested (Li et al., 2015). Peptide 5, which blocks hemichannels at low concentrations and inhibits GJs at higher concentrations, was reported to prevent seizure activity and brain weight loss in fetal sheep following transient bilateral clamping of the carotid arteries (peptide administered directly in brain ventricles; Davidson et al., 2012). While evidence in the literature broadly implicates Cx43 in ischemia, the data presented in this study underscore Cx43 hemichannels as a key focal point in stroke.

We tested this hypothesis by using Gap19, a peptide which has been shown to inhibit astroglial Cx43 hemichannels while not affecting GJ coupling (Abudara et al., 2014). Gap19 is specific to Cx43 and was demonstrated to cross the BBB when coupled to the TAT protein (Abudara et al., 2014). The administration of TAT-Gap19 2 h after pMCAO in WT mice resulted in a significant reduction in infarct volume 4 d after stroke, confirming the hypothesis that Cx43 hemichannels are a major contributing factor to injury in stroke. While Cx43 loop–tail interactions are necessary for hemichannel function, they result in closure of GJs (Leybaert et al., 2017). Thus, preventing loop–tail interaction with L2 or L2-derived peptides was shown to protect against ischemic acidosis-induced GJ closure in cell expression systems (Morley et al., 1996; Verma et al., 2009, 2010), and the Cys-260–Asn-300 region containing three of the four MAPK consensus Ser phosphorylation sites has been proposed, next to others, to be involved in this protection (Morley et al., 1997). However, because GJs were not affected in the MK4 animals, GJ-linked protection does not appear to be involved in the presently used pMCAO model.

While measuring Cx43 expression at different time points would yield a more complete picture, our goal in this study was to investigate a therapeutic window of time where Cx43 activity could be understood and pharmacologically manipulated. We examined two features of Cx43 function that may be potential targets for neuroprotection, specifically, the potential protective benefits provided by GJ coupling and the detrimental hemichannel activity, which may be linked to MAPK

phosphorylation. This study provides significant new insight on the potential therapeutic strategies that revolve around astrocytic Cx43 in brain injury.

Materials and methods

pMCAO

C57BL/6 WT and Cx43-null phosphorylation knock-in mutant mice MK4 Cx43 (Ser-255/262/279/282A; Johnstone et al., 2012), CK1 Cx43 (Ser-325A/328Y/330A), and PKC Cx43 (Ser-368A; Huang et al., 2011) were maintained on a 12:12-h light/dark cycle, with food and water available ad libitum. Male and female WT and mutant mice were subjected to pMCAO, as previously described (Nakase et al., 2004). Briefly, 3–4-mo-old mice were anesthetized with 65 mg/kg sodium pentobarbital (i.p.) and given an opiate (0.1 mg/kg buprenorphine) and a local analgesic (0.1 ml bupivacaine at 0.25%) at incision before surgery. Body temperature was maintained at 37°C during surgery and recovery. The head was held securely in place using a stereotaxic frame (David Kopf Instruments). With the aid of a dissecting microscope (Hund Wetzlar), a skin incision was made on the right side of the head from the anterior of the ear toward the corner of the eye horizontally and from the corner of the eye vertically 5 mm. Using a fine battery-powered drill (Dremel), a small hole was made ∼2 mm in diameter on the skull bone to remove dura and expose the MCA. The MCA was then cauterized above and below the rhinal fissure using an electronic coagulator (Codman & Shurtleff). After visually confirming the absence of reperfusion through the MCA, the skin incision was closed and mice were given a 1-ml subcutaneous bolus of lactate Ringer's solution. After surgery, the mice were monitored for body temperature and maintained at 37°C with a rectal probe until they started to wake up from the anesthetic ∼2 h later, at which time the animals were then placed in their home cages on a heating pad set at 37°C for 12 h. Mice were then transferred to a temperature-controlled (22.0°C) recovery room for the remaining 4 d and monitored daily.

In a separate cohort, WT mice were subjected to the same pMCAO protocol as above; however, after 2 h of ischemia, mice were then given an i.p. injection of saline, 0.75 µmol/kg or 7.5 µmol/kg of the hemichannel blocker TAT-Gap19 (Wang et al., 2013; Abudara et al., 2014), or 7.5 µmol/kg of the inactive scrambled TAT-GAP19. Mice were then euthanized 4 d after pMCAO and brains subjected to histological assessment of infarct volume.

The pMCAO experiments performed in this study conform to the following STAIR requirements. (1) Randomized and blinded studies: our animals were randomly selected and coded for blinded study. (2) Efficacy in two or more laboratories: the first group of pMCAO surgeries was performed at the Fred Hutchinson Cancer Research Center, and the second set of pMCAO surgeries was performed at the University of British Columbia. (3) Consideration of sex difference: male (WT = 4; MK4 = 4) and female (WT = 6; MK4 = 7) infarct volume data were subjected to two-way ANOVA. Two-way analysis indicated a significant main effect of MK4 genotype (F (1, 17) = 11.52; **, P = 0.0035), and main effect of sex (F (1, 17) = 5.204; *, P = 0.0357); however, no significant interaction between sex and genotype (F (1, 17) = 0.4036; P = 0.5337) was observed. (4) Consideration of route of administration: we previously published a study that examined vascular delivery of TAT-Gap19 (Abudara et al., 2014), clearly demonstrating this as an effective route of administration. However, in the current study, we clearly show that Biotin-TAT-Gap19 readily enters the brain following i.p. delivery (Fig. 8). (5) Consideration of a clinically useful therapeutic window and dose response: the therapeutic window considered in our experiments was the administration of TAT-Gap19 2 h after pMCAO. This is within the clinical time frame for the optimal administration of tissue plasminogen activator (Cheng and Kim, 2015). While a formal and complete dose response was not performed in our study, Fig. 8 shows a significant reduction in infarct volume when a 10-fold dilution of TAT-Gap19 is administered 2 h after pMCAO. Finally, if there were hemorrhaging due to poor cauterization, animals were excluded from study. Inclusion was based on visual inspection and confirmation of the MCA occlusion. No mortality occurred during these experiments.

In vivo administration of Biotin-TAT-Gap19

Healthy male C57/B6 mice (84–112 d) received an i.p. injection of 7.5 µmol/kg Biotin-TAT-Gap19 (Pepnome) and were sacrificed 10 or 80 min later through transcardial perfusion with PBS. Following their isolation, brains were immediately snap-frozen in liquid N_2-cooled isopentane and stored at −80°C. 20-µm coronal cryosections were postfixed in 4% paraformaldehyde on glass coverslips for 25 min and permeabilized/blocked in PBS containing 0.2% Triton X-100 and 0.4% porcine skin gelatin for 1 h at room temperature. The sections were then treated with the following primary antibodies: mouse anti-GFAP (1:100 GFAP-Cy3; Sigma-Aldrich), rat anti-CD31 (1:50; Life Technologies Invitrogen), rabbit anti-laminin 1+2 (1:100; Abcam), or rabbit anti-Cx43 (1:100; Sigma-Aldrich). Secondary antibodies (goat anti-rat DyLight 650 and goat anti-rabbit Alexa Fluor 594; Life Technologies Invitrogen) were used at 1:500 dilutions in permeabilization/blocking buffer. Biotinylated TAT-Gap19 was detected using Streptavidin–Alexa Fluor 488 (1:200 in PBS). As a control for endogenous biotin, we also applied Streptavidin–Alexa Fluor 488 to cryosections of animals injected with vehicle only and found no staining. Sections were mounted in Prolong Gold anti-fade reagent containing DAPI. Omission of primary antibodies served as negative controls. Confocal images were acquired on a TCS SP8 laser-scanning confocal microscope equipped with a 63×/1.2 numerical aperture water objective (Leica Microsystem). Colocalization of Biotin-TAT-Gap19 with GFAP, CD31, Laminin, or Cx43 was analyzed using the colocalization plug-in for ImageJ (available at http://rsbweb.nih.gov/ij/).

Quantification of cerebral infarction

Infarct volume was quantified as previously described (Kozoriz et al., 2010). 4 d or 21 d after pMCAO, WT and phosphorylation-null mutant mice were anesthetized using a lethal dose of sodium pentobarbital (120 mg/kg i.p.) and transcardially perfused with PBS, followed by 10% formalin (Sigma-Aldrich). A cryostat (HM 505E; Micron) was used to obtain 20-µm- and 10-µm-thick

sections collected at 100-µm intervals for infarct volume determination and immunocytochemistry. To measure infarct size, sections were stained with 0.125% thionin (Fisher Scientific). Total infarct volumes were calculated using a stereological approach through the rostrocaudal extent of the infarct area and corrected for edema as previously described (Lin et al., 1993). Images were analyzed with ImageJ software.

Immunofluorescence and quantification

We have extensively studied the time course of injury following pMCAO, and 4 d provides an optimal time point to assess not only infarct volume but also neuronal injury and glial reactivity (Nakase et al., 2004). Immunofluorescence was performed as previously described (Freitas-Andrade et al., 2012). Incubation of primary antibodies were performed overnight at 4°C in PBS + 10% goat serum. Primary antibodies and their dilutions used were as follows: rabbit anti-Iba1 (1:400; catalog number 019–19741; Wako) to identify microglial; rabbit anti-GFAP (1:1,000; catalog number G3893; Sigma-Aldrich) to identify astrocytes; Cx43-phospho-Ser-279/Ser-282 (1:1,000, generously provided by P.D. Lampe); and rabbit anti-Cx43 (1:600; catalog number C6219; Sigma-Aldrich). Both Cx43-phospho-Ser-279/Ser-282 and rabbit anti-Cx43 were tested for specificity (Fig. S5). Appropriate secondary Alexa Fluor antibodies (Invitrogen) were used at 1:500 dilutions in PBS buffer. Sections were mounted with Prolong Gold anti-fade reagent with DAPI (Invitrogen). Omission of primary antibodies served as negative controls. Apoptosis was measured with In Situ Cell Death Detection Kit, Fluorescein (Sigma-Aldrich).

Histological quantification was performed as previously described (Freitas-Andrade et al., 2012). At least four mice per genotype (WT and MK4) were analyzed. Four serial brain sections (100-µm intervals) from each animal at the level of the frontal cortex were used for immunofluorescent analysis. Images containing the peri-ischemic area, specifically in the dorsal cortex, were captured by confocal microscopy Leica TCS SP5 II (Leica Nussloch) objectives used: 20×/0.50 PH2-HCX PI Fluortar infinity/0.17/E, and 63×/1.4-0.6 Oil Cs HCX- PL-APO. The Leica LAS AF program was used to acquire images at room temperature (22°C). For quantification of cell numbers, a selected field (960 × 600 µm) encompassing the peri-infarct region of the dorsal cortex was analyzed using ImageJ software. The average of four brain sections per mouse (four mice per genotype) was analyzed and plotted.

Western blot analysis

Protein samples from WT and MK4 cortical tissue as well as cultured astrocytes from both genotypes were resolved by SDS-PAGE as described previously (Freitas-Andrade et al., 2012). Briefly, 40 µg protein was separated on a 12% SDS–polyacrylamide gel and transferred to polyvinylidene difluoride membranes. Membranes were processed and incubated overnight at 4°C with primary antibodies against Cx43 (1:5,000; catalog number C6219; Sigma-Aldrich), Cx43-phospho-Ser-279/Ser-282 (1:1,000, generously provided by P.D. Lampe), MAPK (1:1,000; catalog number 9101; Cell Signaling Technology), and mouse anti-γ-tubulin (1:3,000, catalog number T6557; Sigma-Aldrich) in Tris-buffered saline (Tris 50 mM and NaCl 150 mM, pH 8.0) containing 0.05% Tween (TBST) in 1% nonfat dry milk. The membranes were washed and incubated with horseradish peroxidase–conjugated secondary antibody (Vector Laboratories) 1:5,000 in TBST containing 5% nonfat dry milk. Immunoreactive proteins were visualized by chemiluminescent solution (Super Signal West Pico; Pierce Biotechnology). Densitometric, semiquantitative analysis of Western blots was performed using ImageJ software. Band intensity measurements obtained from proteins of interest were normalized to housekeeping protein (γ-tubulin) values. In addition, individual Western blots were loaded with a standard sample obtained from a mixture of E18 and 9-mo-old ischemic brain homogenates to permit comparisons made between blots.

Astrocyte isolation and in vitro hypoxia

WT and MK4 astrocytes were isolated from early postnatal (P0–P1) cortices as previously described (Le et al., 2014). Dissected cortices were triturated in DMEM (Sigma-Aldrich). The suspension was passed through a 70-µm cell filter and then seeded into flasks (two cortices per T75 flask). Culture media (DMEM supplemented with 10% FBS, 10 U/ml penicillin, and 10 µg/ml streptomycin) was replaced 3 d after plating and every second day thereafter. Before each feeding, cell culture flasks were shaken for 1 min and rinsed twice with media; this reduces microglial contamination to ∼2%. After 7–8 d in vitro, astrocytes were then harvested with trypsin-EDTA (Invitrogen) and frozen in freezing medium (90% FBS and 10% DMSO). Frozen astrocytes were thawed and plated on glass coverslips coated with 0.01% solution poly-L-ornithine (Sigma-Aldrich) or culture dishes. Cultures were maintained for 5–7 d before experiments. All experiments were performed on confluent astrocytes and performed independently at least three times. Astrocytes isolated from different breeding pairs were used for each set of experiments (Le et al., 2014).

WT and MK4 astrocytes were exposed to 3 h of hypoxia as previously described (Orellana et al., 2010) in an artificial cerebrospinal fluid medium that mimics the interstitial ionic concentrations of ischemic brain "ischemic buffer" (Bondarenko and Chesler, 2001; Orellana et al., 2010; in mM: 51 NaCl, 65 K-gluconate, 0.13 $CaCl_2$, 1.5 $MgCl_2$, and 10 Hepes, pH 6.8) containing 27 mM glucose. Hypoxia was induced by placing the cultures inside a hypoxic chamber and removing the air with a CO_2/N_2 (5%/95%) flow that maintained <1.0% oxygen throughout the duration of the experiment. Astrocytes were removed and processed immediately for immunocytochemistry and Western blot analysis.

In situ scrape-loading dye-transfer assay

The scrape-loading assay allows the introduction of a GJ-permeant fluorescent dye, such as LY into cells and to monitor its propagation into GJ-coupled cells within minutes after loading (Desarménien et al., 2013). The scrape-loading experiment performed in this study is a modification of a previously described method (Desarménien et al., 2013). Briefly, WT and MK4 mice were subjected to 2 h of pMCAO. After the 2 h, the mice were euthanized with an overdose of sodium pentobarbital

(120 mg/kg i.p.). The brains were quickly removed and sliced into 350-µm-thick coronal slices with a manual tissue chopper. The coronal slices used for this assay encompass the region of the brain normally affected by our stroke model. The ipsilateral area of the cortex affected by the stroke (parietal-temporal cortex) was then scraped with a 26-gauge needle containing a small mixture (10 µl) of the GJ-permeant fluorescent dye LY (444-D molecular weight [MW]) and GJ-impermeant fluorescent dye dextran rhodamine (10,000-D MW). The same cortical area (parietal-temporal cortex) of the contralateral cortex was similarly treated. After a 50-s incubation, brain slices were immediately fixed in paraformaldehyde (4% in 0.1 M phosphate buffer) and stored at 4°C. Brain slices were then cryosectioned at 10 µm thickness and imaged with an epifluorescence Zeiss Axioplan2 fluorescence microscope (Carl Zeiss). Dye spreading was quantified by measuring the area (in pixels) of LY diffusion subtracted by the area of the GJ-impermeable reference dye, dextran rhodamine, with ImageJ software. In addition, a cohort of control coronal slices was incubated for 5 min with a Cx43 channel blocker, 100 µM CBX, before the scrape-loading assay.

In vitro scrape-loading dye-transfer assay

After hypoxia treatment, dye entry was induced by scraping a confluent monolayer of WT and MK4 astrocytes, incubated with 50 µl of the GJ-permeable dye LY (0.5%) and GJ-impermeable dye dextran-rhodamine (0.05%; 10 kD) in PBS, with a scalpel blade and allowing the dyes to incubate for 2 min. Excess dye was washed off with several rinses of PBS. The extent of coupling was determined by epifluorescence Zeiss Axioplan2 fluorescence microscope at 22°C (objective 16×/0.50 Imm-Plan-NeoFluar, Infinity/0.17) measuring the area (in pixels) of LY diffusion subtracted by the area of the GJ-impermeable reference dye, dextran rhodamine, with ImageJ software (Kozoriz et al., 2013).

Hemichannel assay

Time-lapse fluorescence imaging to measure hemichannel activity was performed as previously described (Kozoriz et al., 2013). WT and MK4 astrocytes in cell culture dishes were washed twice with Locke's solution containing (in mM) 154 NaCl, 5.4 KCl, 2.3 $CaCl_2$, and 5 Hepes, pH 7.4, and incubated in 5 mM ethidium bromide (EtBr). Fluorescence intensity was recorded every 30 s for 10 min to establish background fluorescence with a Zeiss Axioplan2 fluorescence microscope (objective 16×/0.50 Imm-Plan-NeoFluar, Infinity/0.17) at 22°C. To induce hemichannel activity, cells were then switched to Ca^{2+}/Mg^{2+}-free solution, and fluorescence intensity was measured every 30 s for 20 min. Images of ethidium uptake were analyzed with ImageJ software. Each point corresponds to the mean ± SEM of >100 cells in triplicate experiments. Linear regression was performed on a dataset from the Ca^{2+}/Mg^{2+}-free solution portion of the line, and slopes were statistically compared.

Hemichannel activity was also similarly measured in WT and MK4 astrocytes subjected to either control media conditions or 3-h hypoxia followed by 1-h reoxygenation in ischemic buffer conditions according to a previously published report (Orellana et al., 2010).

Electrophysiological recordings of Cx43 hemichannels

Isolated WT and MK4 astrocytes were cultured in DMEM containing 10% heat-inactivated newborn calf serum and 100 U/ml penicillin-streptomycin. When astrocytes became confluent on days 10–15, they were suspended by trypsin-EGTA and replated on glass coverslips for at least 3 h before whole-cell patch-clamp recordings. The procedure yields round shaped and single astrocytes in culture, making stable electrophysiological recordings possible. The treatment did not affect either membrane fraction of connexins or hemichannel activities. The extracellular solution for whole-cell recording consisted of (in mM) 130 NaCl, 10 CsCl, 1 $MgCl_2$, 1.8 Ca^{2+}, 10 Hepes, and 5 glucose (pH 7.4), while the standard whole-cell recording pipette solution was composed of (in mM) 130 CsCl, 10 Na-aspartate, 0.26 $CaCl_2$, 1 $MgCl_2$, 2 EGTA, 7 tetraethylammonium-Cl, and 5 Hepes; pH was adjusted to 7.2. Free Ca^{2+} concentration was 50 nM as calculated with the Webmax Standard software application (Patton, 2003), while the estimations of attained $[Ca^{2+}]_i$ mentioned in the results were also calculated using this software. Whole-cell currents were recorded by an EPC 7 PLUS patch-clamp amplifier (HEKA Electronik). Data were digitized at 3.3 KHz using a NI USB-6221 data acquisition device (National Instruments), and WinWCP acquisition software designed by Dr. J. Dempster (University of Strathclyde, Strathclyde, UK). Measured currents were filtered by a 7-pole Bessel low-pass filter at 1-KHz cutoff frequency. Voltage stimulation consisted of 10-mV incremental voltage steps from −70 to +50 mV with astrocytes initially held at −70 mV.

For single-channel analysis, unitary current events were obtained by subtracting holding currents from the recorded traces. Unitary conductances were calculated from the elementary current transitions Δi as $\gamma = \Delta i/Vm$ followed by construction of all-point conductance histograms that display one or more Gaussian distributions. Channel activity was quantified from the charge transfer Qm through open hemichannels. This is equal to integral of the unitary current traces (i.e., a function of time) over the duration of the voltage steps.

Duolink assay: Immunohistochemistry, image acquisition, and analysis

Astrocytes were fixed in 2% paraformaldehyde for 10 min and permeabilized by 0.2% Triton X-100. Following 1-h incubation with blocking media composed of 5% bovine serum albumin and 10% goat serum, fixed cells were treated with primary antibodies against Cx43 (C-terminal region; produced in rabbit; Sigma-Aldrich) and ZO-1 produced in mouse (Invitrogen, Thermo Fisher Scientific). To detect the subpopulation of Cx43–ZO-1 complexes, Duolink secondary antibodies, PLA probe anti-rabbit MINUS, and anti-mouse PLUS (Sigma-Aldrich) targeting the primary antibodies were applied at 37°C for 1 h. The oligonucleotides conjugated to the probes form a closed circle under the treatment of Duolink ligation assay when the maximum distance between the two target proteins was 40 nm. The resulting closed circles were amplified by polymerase and further recognized by fluorescently labeled oligonucleotides (Duolink In Situ Detection Reagents Red; Sigma-Aldrich) with complementary sequences. A third primary anti-Cx43

(N-terminal) antibody was used to stain the total Cx43 proteins in astrocytes (ABGENT; VWR International). The specificity of the Duolink assay was verified by incubating astrocytes with a CT9 peptide (RPRPDDLEI) conjugated to a membrane-penetrating sequence TAT (180 µM, 2 h) before the fixation. The CT9 peptide, which mimics the C-terminal sequence of Cx43, was previously shown to inhibit the interaction between the Cx43 CT tail and the PDZ2 domain of ZO-1, thereby promoting incorporation of hemichannels into GJ plaques (Palatinus et al., 2012). Cell nuclei were stained with DAPI (1 µg/ml), and the preparations were then mounted in proLong Gold antifade reagent (Thermo Fisher Scientific). Confocal images were acquired on a TCS SP8 laser-scanning confocal microscope equipped with a 63×/1.2 numerical aperture water objective (Leica Microsystems). We defined GJ plaques as green spots with a surface area larger than 0.7 µm^2. The number of colocalized spots between the green GJ signal and red Duolink puncta was quantified using the puncta analyzer plug-in (developed by Bary Wark, available on https://github.com/physion/puncta-analyzer) for NIH ImageJ 2.0 and expressed as the percentage of total GJ plaques that were colocalized with Cx43/ZO1 complexes. This score represents the hemichannel pool linked to ZO-1 scaffolding protein underway for assembly into GJs (Rhett et al., 2011; Rhett and Gourdie, 2012).

Behavioral assessment of forepaw sensory-motor function

The adhesive tape removal test is considered a sensitive and objective method for detecting deficits in forepaw sensation that are commonly found after stroke in the sensorimotor cortex (Bouet et al., 2009; Sweetnam et al., 2012). The behavioral adhesive removal test to assess sensory and motor function of the forepaw was performed as previously described (Bouet et al., 2009; Sweetnam et al., 2012). The adhesive removal test was administered at weekly intervals for 2 wk before pMCAO and 3 wk after pMCAO in both WT and MK4 animals. Briefly, a rectangular piece of tape (4 × 3 mm) was placed on the palm of each forepaw. Mice were then placed in a Plexiglas box and filmed for 120 s, and two observers blind to the condition scored the time taken to remove tape from each paw.

At the end of the experiment, mice were euthanized and the brain assessed histologically for scar tissue volume following the same protocol used to measure infarct volume. Percent loss was evaluated by measuring the average cortical area of ipsilateral and contralateral brain sections, and then the percentage of cortical tissue loss of the ipsilateral with respect to the contralateral for each animal was calculated. We also performed cortical thickness measurements following a protocol recently published (Vetreno et al., 2017). Briefly, vertical cortical thickness through the posterior cingulate cortex was calculated by measuring the distance (in millimeters) from the crest of the genu of the corpus callosum to the outer layer of the dorsal cerebral cortex. Horizontal cortical thickness through the parietal/occipital cortex was calculated by measuring the distance (in millimeters) from the crest of the genu of the corpus callosum to the edge of the lateral cerebral cortex affected by the stroke. Quantification was performed on sections that clearly showed the crest of the genu of the corpus callosum as a reference point for measurements and consistency between samples (bregma 0.74 mm to bregma −1.82 mm). Captured images were assessed using ImageJ software.

Pharmacological tools

CBX disodium was purchased from Tocris Bioscience. Gap19 (KQIEIKKFK; MW 1,161 D), TAT-Gap19 (YGRKKRRQRRR-KQIEIKKFK; MW 2,930 D) and scrambled TAT-Gap19 (YGRKKRRQRRR-IEKFKIKQK) were synthesized by Pepnome (>95% purity). Pep-1 was composed of a TAT-linked sequence coupled to a peptide composed of the Cx43 sequence Asp-245-Pro-283 (YGRKKRRQRRR-DPYHATSGALSPAKDCGSQKYAYF-NGCSSPTAPLSPMSP; Gangoso et al., 2014) and was a kind gift from Dr. A. Tabernero (University of Salamanca, Salamanca, Spain).

Statistics

Animals for surgery and cell isolation were randomly selected, and an experimenter blinded to the genotype performed measurements. Single two-way ANOVA (between two factors) was used to explore most variables of interest, unless the same animal was repeatedly tested over time then a two-way repeated measures ANOVA was used followed by Bonferroni's multiple comparisons test. A one-way ANOVA (one factor) was used to compare multiple means to a single control followed by Bonferroni post hoc test, unless multiple means were compared against each other than Tukey post hoc test was recommended. Unpaired *t* tests were performed when comparing two groups. All P values ≤0.05 were considered statistically significant. Statistical analysis was performed using Prism 6 (Graph Pad). All data are presented as the mean ± SEM.

Study approval

The first group of pMCAO surgeries was performed at the Fred Hutchinson Cancer Research Center (FHCRC), and all animal procedures were approved by the FHCRC Institutional Animal Care and Use Committee. All other pMCAO surgeries were performed at the University of British Columbia and approved by the UBC Animal Care Committee and performed in accordance with the guidelines established by the Canadian Council on Animal Care.

Online supplemental material

Fig. S1 describes in more detail the immunofluorescence quantification used to measure astrocytes and microglial cell number and size. Fig. S2 shows the unique astrocytic phenotype exhibited by MK4 mice 4 d after pMCAO. Fig. S3 demonstrates another method used to measure cortical thickness in WT and MK4 mice 21 d after pMCAO. Fig. S4 shows Biotin-TAT-Gap19 BBB penetration. Fig. S5 demonstrates specificity of phospho-p279/282 Cx43 and rabbit anti-Cx43 antibodies.

Acknowledgments

We thank M. Le Vasseur for constructive comments; A. Williams, D. Lu-Cleary, Y. Khoshnoudian, and W.C. Sin for technical assistance; A. Tabernero (Universidad de Salamanca, Salamanca,

Spain) for her gift of Pep-1 peptide; and G. Lamothe (Department of Mathematics and Statistics, University of Ottawa, Ottawa, Canada) for providing statistical advice.

This work was supported by a Heart and Stroke Foundation of Canada fellowship (to M. Freitas-Andrade), a grant from the Canadian Institutes of Health Research (CIHR), a CIHR team grant on "Vascular Cognitive Impairment: Animal Models of Comorbidity" (to C.C. Naus and M. Freitas-Andrade), the National Institutes of Health (grant GM55632 to P.D. Lampe), the Fund for Scientific Research Flanders, Belgium (grants G.0A82.13N and G0320.15N to L. Leybaert), the Interuniversity Attraction Poles Program (grant P7/10 to L. Leybaert), and Geneeskundige Stichting Koningin Elisabeth (grant STI.DI2.2017.0004.01 to L. Leybaert). C.C. Naus was supported by a Canada Research Chair.

The authors declare no competing financial interests.

Author contributions: M. Freitas-Andrade, J.F. Bechberger, P.D. Lampe, L. Leybaert, and C.C. Naus jointly developed the concept and designed experiments. M. Freitas-Andrade and J.F. Bechberger performed the stroke experiments, including all tissue processing and behavioral studies, and analyzed the data. N. Wang and L. Leybaert carried out and analyzed the electrophysiological and Duolink experiments. M. De Bock characterized and analyzed the penetration and distribution of i.p.-injected Tat-Gap19 in the brain. P.D. Lampe produced initial Cx43 phosphorylation mutant mouse lines, and the initial proof-of-principle experiments were performed in his laboratory. M. Freitas-Andrade wrote the manuscript with input and advice from all authors.

Submitted: 10 August 2017
Revised: 31 March 2018
Accepted: 8 February 2019

References

Abudara, V., J. Bechberger, M. Freitas-Andrade, M. De Bock, N. Wang, G. Bultynck, C.C. Naus, L. Leybaert, and C. Giaume. 2014. The connexin43 mimetic peptide Gap19 inhibits hemichannels without altering gap junctional communication in astrocytes. *Front. Cell. Neurosci.* 8:306. https://doi.org/10.3389/fncel.2014.00306

Belousov, A.B., J.D. Fontes, M. Freitas-Andrade, and C.C. Naus. 2017. Gap junctions and hemichannels: communicating cell death in neurodevelopment and disease. *BMC Cell Biol.* 18(S1, Suppl 1):4. https://doi.org/10.1186/s12860-016-0120-x

Bondarenko, A., and M. Chesler. 2001. Rapid astrocyte death induced by transient hypoxia, acidosis, and extracellular ion shifts. *Glia.* 34:134–142. https://doi.org/10.1002/glia.1048

Bouet, V., M. Boulouard, J. Toutain, D. Divoux, M. Bernaudin, P. Schumann-Bard, and T. Freret. 2009. The adhesive removal test: a sensitive method to assess sensorimotor deficits in mice. *Nat. Protoc.* 4:1560–1564. https://doi.org/10.1038/nprot.2009.125

Burda, J.E., and M.V. Sofroniew. 2014. Reactive gliosis and the multicellular response to CNS damage and disease. *Neuron.* 81:229–248. https://doi.org/10.1016/j.neuron.2013.12.034

Chen, V.C., J.W. Gouw, C.C. Naus, and L.J. Foster. 2013. Connexin multi-site phosphorylation: mass spectrometry-based proteomics fills the gap. *Biochim. Biophys. Acta.* 1828:23–34. https://doi.org/10.1016/j.bbamem.2012.02.028

Chen, W., J. Feng, and W. Tong. 2017. Phosphorylation of astrocytic connexin43 by ERK1/2 impairs blood-brain barrier in acute cerebral ischemia. *Cell Biosci.* 7:43. https://doi.org/10.1186/s13578-017-0170-6

Cheng, N.T., and A.S. Kim. 2015. Intravenous thrombolysis for acute ischemic stroke within 3 hours versus between 3 and 4.5 hours of symptom onset. *Neurohospitalist.* 5:101–109. https://doi.org/10.1177/1941874415583116

Chever, O., C.Y. Lee, and N. Rouach. 2014. Astroglial connexin43 hemichannels tune basal excitatory synaptic transmission. *J. Neurosci.* 34:11228–11232. https://doi.org/10.1523/JNEUROSCI.0015-14.2014

Contreras, J.E., J.C. Sáez, F.F. Bukauskas, and M.V. Bennett. 2003. Gating and regulation of connexin 43 (Cx43) hemichannels. *Proc. Natl. Acad. Sci. USA.* 100:11388–11393. https://doi.org/10.1073/pnas.1434298100

Cui, G.Y., X.M. Gao, S.H. Qi, A. Gillani, L. Gao, X. Shen, and Y.D. Zhang. 2011. The action of thrombin in intracerebral hemorrhage induced brain damage is mediated via PKCα/PKCδ signaling. *Brain Res.* 1398:86–93. https://doi.org/10.1016/j.brainres.2010.11.095

D'hondt, C., J. Iyyathurai, B. Himpens, L. Leybaert, and G. Bultynck. 2014. Cx43-hemichannel function and regulation in physiology and pathophysiology: insights from the bovine corneal endothelial cell system and beyond. *Front. Physiol.* 5:348. https://doi.org/10.3389/fphys.2014.00348

Davidson, J.O., C.R. Green, L.F. Nicholson, S.J. O'Carroll, M. Fraser, L. Bennet, and A.J. Gunn. 2012. Connexin hemichannel blockade improves outcomes in a model of fetal ischemia. *Ann. Neurol.* 71:121–132. https://doi.org/10.1002/ana.22654

del Zoppo, G.J., F.R. Sharp, W.D. Heiss, and G.W. Albers. 2011. Heterogeneity in the penumbra. *J. Cereb. Blood Flow Metab.* 31:1836–1851. https://doi.org/10.1038/jcbfm.2011.93

Demyanenko, S.V., S.N. Panchenko, and A.B. Uzdensky. 2015. Expression of neuronal and signaling proteins in penumbra around a photothrombotic infarction core in rat cerebral cortex. *Biochemistry (Mosc.).* 80:790–799. https://doi.org/10.1134/S0006297915060152

de Pina-Benabou, M.H., V. Szostak, A. Kyrozis, D. Rempe, D. Uziel, M. Urban-Maldonado, S. Benabou, D.C. Spray, H.J. Federoff, P.K. Stanton, and R. Rozental. 2005. Blockade of gap junctions in vivo provides neuroprotection after perinatal global ischemia. *Stroke.* 36:2232–2237. https://doi.org/10.1161/01.STR.0000182239.75969.d8

Desarménien, M.G., C. Jourdan, B. Toutain, E. Vessières, S.G. Hormuzdi, and N.C. Guérineau. 2013. Gap junction signalling is a stress-regulated component of adrenal neuroendocrine stimulus-secretion coupling in vivo. *Nat. Commun.* 4:2938. https://doi.org/10.1038/ncomms3938

Eugenín, E.A., D. Eckardt, M. Theis, K. Willecke, M.V. Bennett, and J.C. Saez. 2001. Microglia at brain stab wounds express connexin 43 and in vitro form functional gap junctions after treatment with interferon-gamma and tumor necrosis factor-alpha. *Proc. Natl. Acad. Sci. USA.* 98:4190–4195. https://doi.org/10.1073/pnas.051634298

Feuerstein, G.Z., X. Wang, and F.C. Barone. 1997. Inflammatory gene expression in cerebral ischemia and trauma. Potential new therapeutic targets. *Ann. N. Y. Acad. Sci.* 825(1 Neuroprotecti):179–193. https://doi.org/10.1111/j.1749-6632.1997.tb48428.x

Freitas-Andrade, M., P. Carmeliet, D.B. Stanimirovic, and M. Moreno. 2008. VEGFR-2-mediated increased proliferation and survival in response to oxygen and glucose deprivation in PlGF knockout astrocytes. *J. Neurochem.* 107:756–767. https://doi.org/10.1111/j.1471-4159.2008.05660.x

Freitas-Andrade, M., P. Carmeliet, C. Charlebois, D.B. Stanimirovic, and M.J. Moreno. 2012. PlGF knockout delays brain vessel growth and maturation upon systemic hypoxic challenge. *J. Cereb. Blood Flow Metab.* 32:663–675. https://doi.org/10.1038/jcbfm.2011.167

Froger, N., J.A. Orellana, C.F. Calvo, E. Amigou, M.G. Kozoriz, C.C. Naus, J.C. Sáez, and C. Giaume. 2010. Inhibition of cytokine-induced connexin43 hemichannel activity in astrocytes is neuroprotective. *Mol. Cell. Neurosci.* 45:37–46. https://doi.org/10.1016/j.mcn.2010.05.007

Gangoso, E., C. Thirant, H. Chneiweiss, J.M. Medina, and A. Tabernero. 2014. A cell-penetrating peptide based on the interaction between c-Src and connexin43 reverses glioma stem cell phenotype. *Cell Death Dis.* 5:e1023. https://doi.org/10.1038/cddis.2013.560

Giaume, C. 1996. [Communicating junctions of glial cells in the central nervous system]. *Ann. Endocrinol. (Paris).* 57:487–491.

Giaume, C., L. Leybaert, C.C. Naus, and J.C. Sáez. 2013. Connexin and pannexin hemichannels in brain glial cells: properties, pharmacology, and roles. *Front. Pharmacol.* 4:88. https://doi.org/10.3389/fphar.2013.00088

Goodenough, D.A., and D.L. Paul. 2009. Gap junctions. *Cold Spring Harb. Perspect. Biol.* 1:a002576. https://doi.org/10.1101/cshperspect.a002576

Huang, G.Y., L.J. Xie, K.L. Linask, C. Zhang, X.Q. Zhao, Y. Yang, G.M. Zhou, Y. J. Wu, L. Marquez-Rosado, D.B. McElhinney, et al. 2011. Evaluating the role of connexin43 in congenital heart disease: Screening for mutations in patients with outflow tract anomalies and the analysis of knock-in mouse models. *J. Cardiovasc. Dis. Res.* 2:206–212. https://doi.org/10.4103/0975-3583.89804

Ito, D., K. Tanaka, S. Suzuki, T. Dembo, and Y. Fukuuchi. 2001. Enhanced expression of Iba1, ionized calcium-binding adapter molecule 1, after transient focal cerebral ischemia in rat brain. *Stroke.* 32:1208–1215. https://doi.org/10.1161/01.STR.32.5.1208

Iyyathurai, J., N. Wang, C. D'Hondt, J.X. Jiang, L. Leybaert, and G. Bultynck. 2018. The SH3-binding domain of Cx43 participates in loop/tail interactions critical for Cx43-hemichannel activity. *Cell. Mol. Life Sci.* 75: 2059–2073.

Jiang, Z., Y. Zhang, X. Chen, P.Y. Lam, H. Yang, Q. Xu, and A.C. Yu. 2002. Activation of Erk1/2 and Akt in astrocytes under ischemia. *Biochem. Biophys. Res. Commun.* 294:726–733. https://doi.org/10.1016/S0006-291X(02)00540-5

Jin, C., K.D. Martyn, W.E. Kurata, B.J. Warn-Cramer, and A.F. Lau. 2004. Connexin43 PDZ2 binding domain mutants create functional gap junctions and exhibit altered phosphorylation. *Cell Commun. Adhes.* 11: 67–87. https://doi.org/10.1080/15419060490951781

Johnstone, S.R., B.M. Kroncke, A.C. Straub, A.K. Best, C.A. Dunn, L.A. Mitchell, Y. Peskova, R.K. Nakamoto, M. Koval, C.W. Lo, et al. 2012. MAPK phosphorylation of connexin 43 promotes binding of cyclin E and smooth muscle cell proliferation. *Circ. Res.* 111:201–211. https://doi.org/10.1161/CIRCRESAHA.112.272302

Kamphuis, W., L. Kooijman, M. Orre, O. Stassen, M. Pekny, and E.M. Hol. 2015. GFAP and vimentin deficiency alters gene expression in astrocytes and microglia in wild-type mice and changes the transcriptional response of reactive glia in mouse model for Alzheimer's disease. *Glia.* 63:1036–1056. https://doi.org/10.1002/glia.22800

Kaneko, N., J.Y. Hwang, M. Gertner, F. Pontarelli, and R.S. Zukin. 2014. Casein kinase 1 suppresses activation of REST in insulted hippocampal neurons and halts ischemia-induced neuronal death. *J. Neurosci.* 34: 6030–6039. https://doi.org/10.1523/JNEUROSCI.4045-13.2014

Kozoriz, M.G., J.F. Bechberger, G.R. Bechberger, M.W. Suen, A.P. Moreno, K. Maass, K. Willecke, and C.C. Naus. 2010. The connexin43 C-terminal region mediates neuroprotection during stroke. *J. Neuropathol. Exp. Neurol.* 69:196–206. https://doi.org/10.1097/NEN.0b013e3181cd44df

Kozoriz, M.G., S. Lai, J.L. Vega, J.C. Sáez, W.C. Sin, J.F. Bechberger, and C.C. Naus. 2013. Cerebral ischemic injury is enhanced in a model of oculodentodigital dysplasia. *Neuropharmacology.* 75:549–556. https://doi.org/10.1016/j.neuropharm.2013.05.003

Kraft, A.W., X. Hu, H. Yoon, P. Yan, Q. Xiao, Y. Wang, S.C. Gil, J. Brown, U. Wilhelmsson, J.L. Restivo, et al. 2013. Attenuating astrocyte activation accelerates plaque pathogenesis in APP/PS1 mice. *FASEB J.* 27:187–198. https://doi.org/10.1096/fj.12-208660

Laird, D.W. 1996. The life cycle of a connexin: gap junction formation, removal, and degradation. *J. Bioenerg. Biomembr.* 28:311–318. https://doi.org/10.1007/BF02110107

Le, H.T., W.C. Sin, S. Lozinsky, J. Bechberger, J.L. Vega, X.Q. Guo, J.C. Sáez, and C.C. Naus. 2014. Gap junction intercellular communication mediated by connexin43 in astrocytes is essential for their resistance to oxidative stress. *J. Biol. Chem.* 289:1345–1354. https://doi.org/10.1074/jbc.M113.508390

Leybaert, L., P.D. Lampe, S. Dhein, B.R. Kwak, P. Ferdinandy, E.C. Beyer, D.W. Laird, C.C. Naus, C.R. Green, and R. Schulz. 2017. Connexins in cardiovascular and neurovascular health and disease: Pharmacological implications. *Pharmacol. Rev.* 69:396–478. https://doi.org/10.1124/pr.115.012062

Li, L., A. Lundkvist, D. Andersson, U. Wilhelmsson, N. Nagai, A.C. Pardo, C. Nodin, A. Ståhlberg, K. Aprico, K. Larsson, et al. 2008. Protective role of reactive astrocytes in brain ischemia. *J. Cereb. Blood Flow Metab.* 28: 468–481. https://doi.org/10.1038/sj.jcbfm.9600546

Li, W.E., P.A. Ochalski, E.L. Hertzberg, and J.I. Nagy. 1998. Immunorecognition, ultrastructure and phosphorylation status of astrocytic gap junctions and connexin43 in rat brain after cerebral focal ischaemia. *Eur. J. Neurosci.* 10: 2444–2463. https://doi.org/10.1046/j.1460-9568.1998.00253.x

Li, X., H. Zhao, X. Tan, R.M. Kostrzewa, G. Du, Y. Chen, J. Zhu, Z. Miao, H. Yu, J. Kong, and X. Xu. 2015. Inhibition of connexin43 improves functional recovery after ischemic brain injury in neonatal rats. *Glia.* 63:1553–1567. https://doi.org/10.1002/glia.22826

Lin, T.N., Y.Y. He, G. Wu, M. Khan, and C.Y. Hsu. 1993. Effect of brain edema on infarct volume in a focal cerebral ischemia model in rats. *Stroke.* 24: 117–121. https://doi.org/10.1161/01.STR.24.1.117

Lucke-Wold, B.P., R.C. Turner, A.F. Logsdon, J.W. Simpkins, D.L. Alkon, K.E. Smith, Y.W. Chen, Z. Tan, J.D. Huber, and C.L. Rosen. 2015. Common mechanisms of Alzheimer's disease and ischemic stroke: the role of protein kinase C in the progression of age-related neurodegeneration. *J. Alzheimers Dis.* 43:711–724. https://doi.org/10.3233/JAD-141422

Márquez-Rosado, L., J.L. Solan, C.A. Dunn, R.P. Norris, and P.D. Lampe. 2012. Connexin43 phosphorylation in brain, cardiac, endothelial and epithelial tissues. *Biochim. Biophys. Acta.* 1818:1985–1992. https://doi.org/10.1016/j.bbamem.2011.07.028

Morley, G.E., S.M. Taffet, and M. Delmar. 1996. Intramolecular interactions mediate pH regulation of connexin43 channels. *Biophys. J.* 70:1294–1302. https://doi.org/10.1016/S0006-3495(96)79686-8

Morley, G.E., J.F. Ek-Vitorín, S.M. Taffet, and M. Delmar. 1997. Structure of connexin43 and its regulation by pHi. *J. Cardiovasc. Electrophysiol.* 8: 939–951. https://doi.org/10.1111/j.1540-8167.1997.tb00856.x

Nakase, T., S. Fushiki, and C.C. Naus. 2003. Astrocytic gap junctions composed of connexin 43 reduce apoptotic neuronal damage in cerebral ischemia. *Stroke.* 34:1987–1993. https://doi.org/10.1161/01.STR.0000079814.72027.34

Nakase, T., G. Söhl, M. Theis, K. Willecke, and C.C. Naus. 2004. Increased apoptosis and inflammation after focal brain ischemia in mice lacking connexin43 in astrocytes. *Am. J. Pathol.* 164:2067–2075. https://doi.org/10.1016/S0002-9440(10)63765-0

Naus, C.C., J.F. Bechberger, S. Caveney, and J.X. Wilson. 1991. Expression of gap junction genes in astrocytes and C6 glioma cells. *Neurosci. Lett.* 126: 33–36. https://doi.org/10.1016/0304-3940(91)90364-Y

Naus, C.C., M.A. Ozog, J.F. Bechberger, and T. Nakase. 2001. A neuroprotective role for gap junctions. *Cell Commun. Adhes.* 8:325–328. https://doi.org/10.3109/15419060109080747

Nimlamool, W., R.M. Andrews, and M.M. Falk. 2015. Connexin43 phosphorylation by PKC and MAPK signals VEGF-mediated gap junction internalization. *Mol. Biol. Cell.* 26:2755–2768. https://doi.org/10.1091/mbc.E14-06-1105

Orellana, J.A., P.J. Sáez, K.F. Shoji, K.A. Schalper, N. Palacios-Prado, V. Velarde, C. Giaume, M.V. Bennett, and J.C. Sáez. 2009. Modulation of brain hemichannels and gap junction channels by pro-inflammatory agents and their possible role in neurodegeneration. *Antioxid. Redox Signal.* 11:369–399. https://doi.org/10.1089/ars.2008.2130

Orellana, J.A., D.E. Hernández, P. Ezan, V. Velarde, M.V. Bennett, C. Giaume, and J.C. Sáez. 2010. Hypoxia in high glucose followed by reoxygenation in normal glucose reduces the viability of cortical astrocytes through increased permeability of connexin 43 hemichannels. *Glia.* 58:329–343.

Orellana, J.A., K.F. Shoji, V. Abudara, P. Ezan, E. Amigou, P.J. Sáez, J.X. Jiang, C.C. Naus, J.C. Sáez, and C. Giaume. 2011. Amyloid β-induced death in neurons involves glial and neuronal hemichannels. *J. Neurosci.* 31: 4962–4977. https://doi.org/10.1523/JNEUROSCI.6417-10.2011

Orellana, J.A., R. von Bernhardi, C. Giaume, and J.C. Sáez. 2012. Glial hemichannels and their involvement in aging and neurodegenerative diseases. *Rev. Neurosci.* 23:163–177. https://doi.org/10.1515/revneuro-2011-0065

Ozog, M.A., R. Siushansian, and C.C. Naus. 2002. Blocked gap junctional coupling increases glutamate-induced neurotoxicity in neuron-astrocyte co-cultures. *J. Neuropathol. Exp. Neurol.* 61:132–141. https://doi.org/10.1093/jnen/61.2.132

Palatinus, J.A., J.M. Rhett, and R.G. Gourdie. 2012. The connexin43 carboxyl terminus and cardiac gap junction organization. *Biochim. Biophys. Acta.* 1818:1831–1843. https://doi.org/10.1016/j.bbamem.2011.08.006

Patton, C. 2003. WEBMAXC Standard. Available at http://www.stanford.edu/~cpatton/webmaxcS.htm (accessed September 2017).

Perez Velazquez, J.L., L. Kokarovtseva, R. Sarbaziha, Z. Jeyapalan, and Y. Leshchenko. 2006. Role of gap junctional coupling in astrocytic networks in the determination of global ischaemia-induced oxidative stress and hippocampal damage. *Eur. J. Neurosci.* 23:1–10. https://doi.org/10.1111/j.1460-9568.2005.04523.x

Pogoda, K., P. Kameritsch, M.A. Retamal, and J.L. Vega. 2016. Regulation of gap junction channels and hemichannels by phosphorylation and redox changes: a revision. *BMC Cell Biol.* 17(S1, Suppl 1):11. https://doi.org/10.1186/s12860-016-0099-3

Ponsaerts, R., E. De Vuyst, M. Retamal, C. D'hondt, D. Vermeire, N. Wang, H. De Smedt, P. Zimmermann, B. Himpens, J. Vereecke, et al. 2010. Intramolecular loop/tail interactions are essential for connexin 43-hemichannel activity. *FASEB J.* 24:4378–4395. https://doi.org/10.1096/fj.09-153007

Rami, A., T. Volkmann, and J. Winckler. 2001. Effective reduction of neuronal death by inhibiting gap junctional intercellular communication in a rodent model of global transient cerebral ischemia. *Exp. Neurol.* 170: 297–304. https://doi.org/10.1006/exnr.2001.7712

Rawanduzy, A., A. Hansen, T.W. Hansen, and M. Nedergaard. 1997. Effective reduction of infarct volume by gap junction blockade in a rodent model of stroke. *J. Neurosurg.* 87:916–920. https://doi.org/10.3171/jns.1997.87.6.0916

Retamal, M.A., N. Froger, N. Palacios-Prado, P. Ezan, P.J. Sáez, J.C. Sáez, and C. Giaume. 2007. Cx43 hemichannels and gap junction channels in

astrocytes are regulated oppositely by proinflammatory cytokines released from activated microglia. *J. Neurosci.* 27:13781–13792. https://doi.org/10.1523/JNEUROSCI.2042-07.2007

Rhett, J.M., and R.G. Gourdie. 2012. The perinexus: a new feature of Cx43 gap junction organization. *Heart Rhythm.* 9:619–623. https://doi.org/10.1016/j.hrthm.2011.10.003

Rhett, J.M., J. Jourdan, and R.G. Gourdie. 2011. Connexin 43 connexon to gap junction transition is regulated by zonula occludens-1. *Mol. Biol. Cell.* 22: 1516–1528. https://doi.org/10.1091/mbc.e10-06-0548

Sacco, R.L., S.E. Kasner, J.P. Broderick, L.R. Caplan, J.J. Connors, A. Culebras, M. S. Elkind, M.G. George, A.D. Hamdan, R.T. Higashida, et al.; Council on Nutrition, Physical Activity and Metabolism. 2013. An updated definition of stroke for the 21st century: a statement for healthcare professionals from the American Heart Association/American Stroke Association. *Stroke.* 44:2064–2089. https://doi.org/10.1161/STR.0b013e318296aeca

Saffitz, J.E., J.G. Laing, and K.A. Yamada. 2000. Connexin expression and turnover : implications for cardiac excitability. *Circ. Res.* 86:723–728. https://doi.org/10.1161/01.RES.86.7.723

Saito, R., R. Graf, K. Hübel, T. Fujita, G. Rosner, and W.D. Heiss. 1997. Reduction of infarct volume by halothane: effect on cerebral blood flow or perifocal spreading depression-like depolarizations. *J. Cereb. Blood Flow Metab.* 17: 857–864. https://doi.org/10.1097/00004647-199708000-00004

Sawe, N., G. Steinberg, and H. Zhao. 2008. Dual roles of the MAPK/ERK1/2 cell signaling pathway after stroke. *J. Neurosci. Res.* 86:1659–1669. https://doi.org/10.1002/jnr.21604

Schulz, R., P.M. Görge, A. Görbe, P. Ferdinandy, P.D. Lampe, and L. Leybaert. 2015. Connexin 43 is an emerging therapeutic target in ischemia/reperfusion injury, cardioprotection and neuroprotection. *Pharmacol. Ther.* 153:90–106. https://doi.org/10.1016/j.pharmthera.2015.06.005

Sirnes, S., A. Kjenseth, E. Leithe, and E. Rivedal. 2009. Interplay between PKC and the MAP kinase pathway in Connexin43 phosphorylation and inhibition of gap junction intercellular communication. *Biochem. Biophys. Res. Commun.* 382:41–45. https://doi.org/10.1016/j.bbrc.2009.02.141

Siushansian, R., J.F. Bechberger, D.F. Cechetto, V.C. Hachinski, and C.C. Naus. 2001. Connexin43 null mutation increases infarct size after stroke. *J. Comp. Neurol.* 440:387–394. https://doi.org/10.1002/cne.1392

Solan, J.L., and P.D. Lampe. 2009. Connexin43 phosphorylation: structural changes and biological effects. *Biochem. J.* 419:261–272. https://doi.org/10.1042/BJ20082319

Sun, J., and G. Nan. 2016. The mitogen-activated protein kinase (MAPK) signaling pathway as a discovery target in stroke. *J. Mol. Neurosci.* 59: 90–98. https://doi.org/10.1007/s12031-016-0717-8

Sweetnam, D., A. Holmes, K.A. Tennant, A. Zamani, M. Walle, P. Jones, C. Wong, and C.E. Brown. 2012. Diabetes impairs cortical plasticity and functional recovery following ischemic stroke. *J. Neurosci.* 32:5132–5143. https://doi.org/10.1523/JNEUROSCI.5075-11.2012

Verma, V., B.D. Larsen, W. Coombs, X. Lin, G. Spagnol, P.L. Sorgen, S.M. Taffet, and M. Delmar. 2009. Novel pharmacophores of connexin43 based on the "RXP" series of Cx43-binding peptides. *Circ. Res.* 105: 176–184. https://doi.org/10.1161/CIRCRESAHA.109.200576

Verma, V., B.D. Larsen, W. Coombs, X. Lin, E. Sarrou, S.M. Taffet, and M. Delmar. 2010. Design and characterization of the first peptidomimetic molecule that prevents acidification-induced closure of cardiac gap junctions. *Heart Rhythm.* 7:1491–1498. https://doi.org/10.1016/j.hrthm.2010.06.028

Vetreno, R.P., R. Yaxley, B. Paniagua, G.A. Johnson, and F.T. Crews. 2017. Adult rat cortical thickness changes across age and following adolescent intermittent ethanol treatment. *Addict. Biol.* 22:712–723. https://doi.org/10.1111/adb.12364

Wallraff, A., R. Köhling, U. Heinemann, M. Theis, K. Willecke, and C. Steinhäuser. 2006. The impact of astrocytic gap junctional coupling on potassium buffering in the hippocampus. *J. Neurosci.* 26:5438–5447. https://doi.org/10.1523/JNEUROSCI.0037-06.2006

Wang, N., M. De Bock, G. Antoons, A.K. Gadicherla, M. Bol, E. Decrock, W.H. Evans, K.R. Sipido, F.F. Bukauskas, and L. Leybaert. 2012. Connexin mimetic peptides inhibit Cx43 hemichannel opening triggered by voltage and intracellular Ca2+ elevation. *Basic Res. Cardiol.* 107:304. https://doi.org/10.1007/s00395-012-0304-2

Wang, N., E. De Vuyst, R. Ponsaerts, K. Boengler, N. Palacios-Prado, J. Wauman, C.P. Lai, M. De Bock, E. Decrock, M. Bol, et al. 2013. Selective inhibition of Cx43 hemichannels by Gap19 and its impact on myocardial ischemia/reperfusion injury. *Basic Res. Cardiol.* 108:309. https://doi.org/10.1007/s00395-012-0309-x

Warn-Cramer, B.J., G.T. Cottrell, J.M. Burt, and A.F. Lau. 1998. Regulation of connexin-43 gap junctional intercellular communication by mitogen-activated protein kinase. *J. Biol. Chem.* 273:9188–9196. https://doi.org/10.1074/jbc.273.15.9188

Warner, D.S., P.S. Ludwig, R. Pearlstein, and A.D. Brinkhous. 1995. Halothane reduces focal ischemic injury in the rat when brain temperature is controlled. *Anesthesiology.* 82:1237–1245.

Wu, D.C., W. Ye, X.M. Che, and G.Y. Yang. 2000. Activation of mitogen-activated protein kinases after permanent cerebral artery occlusion in mouse brain. *J. Cereb. Blood Flow Metab.* 20:1320–1330. https://doi.org/10.1097/00004647-200009000-00007